Article:

Meza, F.J., Becque, J. and Hajirasouliha, I. orcid.org/0000-0003-2597-8200 (2020) Experimental study of the cross-sectional capacity of cold-formed steel built-up columns. Thin-Walled Structures, 155. 106958. ISSN 0263-8231

https://doi.org/10.1016/j.tws.2020.106958

EXPERIMENTAL STUDY OF THE CROSS-SECTIONAL CAPACITY OF COLD-FORMED STEEL BUILT-UP COLUMNS

Francisco J. Meza [a], Jurgen Becque [a] and Iman Hajirasouliha [a]

[a] Department of Civil and Structural Engineering, The University of Sheffield, Sheffield, UK

Abstract: This paper describes a comprehensive experimental programme in which built-up cold-formed steel stub columns with four different cross-sectional geometries were investigated. Twenty built-up sections were fabricated from individual channels and flat plates with nominal thicknesses ranging from 1.2 mm to 2.4 mm and assembled with either bolts or self-drilling screws. The connector spacing was varied among specimens of the same geometry in order to study its effect. The built-up columns were tested between fixed boundary conditions and the load was transmitted through end plates which were attached to the columns with an epoxy resin. Tensile coupons were taken from the corners and flat portions of the constituent sections in order to determine their material properties, while detailed measurements of the geometric imperfections of each specimen were also performed using a laser displacement sensor. The experiments revealed a significant amount of restraint and interaction between the individual components of the columns while buckling, with the connector spacing having a pronounced effect on the observed buckling modes. However, the ultimate cross-sectional capacity was seen to be much less dependent on the connector spacing within the considered range of spacings.

Keywords: Built-up column; Experiment; Cold-formed steel; Stability; Buckling; Imperfection measurements.

1. Introduction

Cold-formed steel (CFS) sections offer many important benefits to construction, such as high strength-to-weight and stiffness-to-weight ratios, an ease of handling, transportation and stacking, and important sustainability credentials due to their recyclability and efficient material use. For these reasons their range of application has rapidly expanded from being mainly used as secondary members in steel structures to an increasing use as primary members. Examples are multi-storey buildings constructed entirely out of CFS [1] and CFS portal frames [2]. This trend in construction is exerting an increased demand on CFS structural members in terms of the span length and the load carrying capacity they need to provide. One way of meeting these increased requirements is by joining two or more sections together by means of welding or fasteners such as bolts, rivets or screws, to form a built-up section. A wider range of cross-sectional shapes can thus be obtained using the currently available single shapes and cross-sections can be tailored to meet specific requirements. In addition, double symmetry, which is difficult to obtain in single CFS sections, can easily be achieved, while closed sections with increased torsional resistance can also readily be constructed. However, a gap in understanding of the way these sections behave and a lack of specific design provisions in the current design codes (e.g. AISI S100 [3]; EN 1993-1-3 [4]) has prevented the exploitation of their full potential. Designing a built-up section requires careful consideration of various factors, including the type of connector used, the spacing between connectors, the degree to which the individual components work as one cross-section, and the occurrence of individual as well as coupled instabilities.

CFS built-up members have already attracted significant research interest, especially during the past decade. With regard to built-up compression members, most of the previous research has focused on either I-shaped cross-sections constructed by connecting two identical channels or sigma sections through their webs in a back-to-back configuration, or built-up closed sections obtained by connecting channel sections through their flanges. These types of cross-sections are commonly found in CFS roof trusses and framing systems used in multi-storey buildings. Research on CFS I-shaped built-up columns includes the experimental work presented by Stone and LaBoube [5], where the specimens were constructed from lipped channels connected with screws. The specimens were seated in track sections at each end in order to replicate the usual end conditions encountered in CFS framing systems. More recently, Fratamico et al. [6] also tested I-shaped columns seated in tracks. However, the researchers added a group of connectors at each end of the column, as prescribed in AISI S100 [3], to study its effect on the amount of composite action achieved in the columns. Lu et al. [7] also conducted noteworthy research on screw-connected back-to-back lipped channel columns. In this latter experimental programme endplates were welded to the column, avoiding any possible end slip between the components. The authors observed that a significant amount of composite action could be achieved when the failure mode was governed by global buckling, while composite action could be disregarded when the failure mode of the tested columns was predominantly local or distortional buckling. Zhang and Young [8] conducted compression tests on I-shaped built-up columns constructed from lipped sigma sections. The specimens were assembled with self-tapping screws and were designed to exhibit local, distortional and global buckling, as well as interaction between these buckling modes. The tests suggested that some degree of composite behaviour was present. Abbasi et al. [9] further investigated this built-up geometry by carrying out a stability analysis using the compound strip method to study the effect of the connector spacing on the buckling behaviour of the columns, and showed that reducing the connector spacing enhanced the elastic local and global buckling stresses of the built-up member.

An experimental investigation on screw-connected built-up columns with various geometries, including open and closed sections, assembled from up to four individual channels, was conducted in [10]. The built-up specimens were tested with pin-ended or fixed-ended boundary conditions and failed by interaction between cross-sectional and global buckling. The study revealed a significant degree of composite action, with the built-up geometries exhibiting ultimate capacities larger than those obtained by simply adding up the contributions of the individual components. Liao et al. [11] carried out an experimental and numerical investigation of multi-limb built-up stub columns with geometries similar to those tested in [10] and found that the connector spacing had little impact on the ultimate capacity of the stub columns. Compression tests on simply supported built-up closed sections assembled from lipped channels welded together at regular intervals in a toe-to-toe configuration were carried out in [12]. The investigated cross-sections were relatively stocky and the specimens failed due to global instabilities without the presence of local buckling. Reyes and Guzmán [13] carried out experiments on built-up closed section columns of similar geometry, but employed channels with more slender cross-sections. The specimens were tested between either fixed or flexible support conditions, and were relatively short, failing predominantly due to local buckling. The tests showed no statistical reduction in the ultimate capacity due to a larger connector spacing when failure was governed by local buckling. Young and Chen [14] and Zhang and Young [15] experimentally studied screw-connected built-up closed sections assembled from two identical sigma sections or channel sections, respectively. The columns were tested between fixed end conditions, with endplates welded to each end, and their failure modes involved local, distortional and global flexural buckling. The tests showed that the ultimate capacity of the built-up members was generally larger than that obtained by simply adding the contributions of the individual channels. Li et al. [16] also carried out compression tests on built-up closed section columns assembled from lipped channels with intermediate web stiffeners. However, the specimens were tested without welded endplates, resulting in some of the specimens failing prematurely due to an uneven distribution of the load between the components. Georgieva et al. [17-20] carried out an extensive experimental and numerical investigation to study the buckling behaviour of double-Z built-up columns. The columns were assembled with spacers bolted to both Z-sections to restrain distortion of the cross-section at discrete points and were designed to exhibit local, distortional and global buckling.

A simple design equation was proposed in [21] to predict the ultimate capacity of I-shaped and closed section built-up columns assembled from lipped channels stitch-welded together at various spacings and failing by distortional or global flexural buckling. The equation was based on the experimental and numerical data gathered in [12,22,23]. However, the authors suggested that more compression tests on other practical built-up geometries were needed to further validate the proposed equation.

Despite the significant amount of research focused on built-up compression members to date, most of the previously investigated geometries were fabricated from two identical components, with both components buckling at the same time. In contrast to this, the experimental programme described in this paper consisted of 20 stub column tests of four different built-up geometries, each constructed from four individual components including two different cross-sections. The cross-sectional components were brake-pressed from galvanized steel sheet with thicknesses between 1.2 mm and 2.4 mm and were connected with either M6 bolts or M5.5 self-drilling screws. The aim of the study was to investigate the cross-sectional compressive behaviour and capacity of the tested geometries and quantify the influence of parameters specific to built-up sections. Most importantly, the effect of the longitudinal connector spacing on the cross-sectional stability and the ultimate capacity of the built-up specimens was investigated. Direct observations from the tests, as well as comparisons of the measured buckling loads with those calculated for isolated components, also provided information about the mutual restraint components offered to each other in the built-up configuration through contact and discrete connections. The targeted instabilities were local buckling of the components, as well as (overall) buckling of the components in between connection points. Previous related research by the authors has also covered the behaviour and capacity of CFS built-up beams [24] and CFS built-up long columns [25].

2. Section geometry and specimen fabrication

Figure 1 illustrates the four cross-sectional geometries included in the tests. The individual components were brake-pressed by an external fabricator and were given a specific label. Plain channels, lipped channels and flat plate components were labelled using the letters '*T*', '*S*' or '*P*', respectively, followed by the nominal height of their web in mm (in the case of the channels) or the nominal width of the plate in mm, and the nominal wall thickness in mm multiplied by 10. To refer to each built-up specimen, the letters '*SC*' were used to indicate that the specimen was a stub column, followed by a number ranging from 1 to 4 to indicate its cross-sectional geometry (with reference to Figure 1), a hyphen and the number of rows of intermediate connectors (i.e. not counting the connectors in the end sections). As each test was repeated, the letters '*a*' and '*b*' were used to indicate whether the specimen was the first or the second of twin columns tested. For example, the label '*SC1-2a*' referred to the first stub column tested with cross-section geometry 1 which contained two intermediate rows of connectors between the end connectors.

Sections P20024, T15414 and T7912 (i.e. those used to assemble columns SC1 and SC2) were manufactured from pre-galvanized steel sheets with a guaranteed yield stress of 450 MPa and a Z275 zinc coating with a total nominal thickness of 0.04 mm. Sections T12012 and S11012 (i.e. those used to assemble columns SC3 and SC4) had a guaranteed yield stress of 260 MPa, and although for these sections the coating thickness was not specified by the manufacturer, it was determined to be 0.03 mm by measuring the thickness of the sections at each end before and after removing the zinc coating with hydrochloric acid. The thickness of the sections was measured using a digital micrometre with a precision of ±0.002 mm, while the rest of the dimensional measurements were carried out using a digital Vernier caliper with a precision of ±0.03 mm. All measurements were of the outside dimensions, as illustrated in Figure 2. Table 1 lists the nominal dimensions of the components (using the symbols introduced in Figure 2), while Tables 2-5 summarize the measured dimensions for columns SC1-SC4, respectively. Each listed value is the average result of several measurements taken at different locations. The thickness values correspond to the base metal and were obtained after deducting the thickness of the zinc coating.

All stub columns were designed to fail by cross-sectional instability, buckling of the individual components between connectors, or a combination of both, but without influence of global instabilities. In this respect the recommendations of the 'Column Research Council' were followed, which state that the length of the column should be larger than three times the largest dimension of the cross-section and smaller than 20 times the least radius of gyration [26]. As a result, the length chosen for columns SC1, SC3 and SC4 was 1100 mm and the length of columns SC2 was 800 mm. At these lengths, all columns were expected to buckle with at least six half-waves along their length. This resulted in at least one buckling wave (in the middle) where the influence of the boundary conditions was minimal. An estimate of the local bucking load was obtained by carrying out a finite strip analysis of the column components, considered in isolation without contact or connections with the other components, using CUFSM [27]. Flexural buckling of the flat plates between connector points in columns SC1 was predicted using the classical (elastic) equation, using a buckling length equal to half the connector spacing.

The connector spacing was varied among specimens of the same geometry in order to study its influence. Columns SC1 were designed with 2, 3 and 5 equally spaced intermediate rows of connectors, corresponding to configurations where the predicted flexural buckling stress of the flat plates was lower than, equal to and higher than the predicted local buckling stress of the channels, respectively. Columns SC2 were designed with 2, 4 and 6 rows, and columns SC3 and SC4 were designed with 2 and 5 rows, as shown in Figure 3. These connector spacings were chosen based on the predicted local buckling half-wavelengths of the components. In columns SC2-6 the connector spacing was shorter than twice the natural half-wavelength of the channels, while in columns SC2-2 the connector spacing was larger. In columns SC3-5 and SC4-5 the connector spacing coincided with twice the natural local buckling half-wavelength of the lipped channels, but was shorter than twice the half-wavelength of the plain channels, while in columns SC3-2 and SC4-2 the connector spacing was larger than twice the natural half-wavelength of all channels.

The test specimens were constructed using two different types of connectors, to study whether this influenced their behaviour. Columns SC1 and SC2 were assembled using M6 bolts, while columns SC3 and SC4 were assembled using M5.5 self-drilling sheet metal screws (Figure 4). For more detailed considerations regarding the design of the test specimens the reader is referred to [28].

In order to assemble columns SC1 and SC2, bolt holes with a diameter of 6.25 mm were drilled in the appropriate locations. In columns SC1, the holes were first drilled in the flat plate components at the locations shown in Figure 3a. For columns SC2, the holes were first drilled in the outer channels at the locations illustrated in Figure 3b. These sections were then used as templates to drill the holes in the remaining sections after positioning all sections in their built-up configuration and securing them with clamps. The components were then bolted together using a torque wrench, while applying a torque of 10 Nm. This value was judged to be representative of manually tightening the bolts with a spanner. A similar procedure was followed to assemble columns SC3 and SC4. The locations of the screws were first marked in one of the connecting components and small diameter holes were drilled in order to facilitate the installation of the screws. Next, the sections were positioned in their built-up configuration, secured with clamps and screwed together. The locations of the screws are illustrated in Figure 3c and**Error! Reference source not found.** Figure 3d for columns SC3 and SC4, respectively. Figures 5a-c show the finalized columns SC1-SC4.

After the assembly process, both ends of each column were manually filed to correct any differences in length between the individual components. Much care was put into this process to ensure that a completely even bearing surface was obtained between the specimen ends and the end plates. Endplates with dimensions of 250×300 mm^2 and a thickness of 20 mm were then attached to both ends of columns SC1 and SC2, while endplates with dimensions of 200×200 mm^2 and a thickness of 20 mm were attached to the ends of columns SC3 and SC4. It was decided not to weld the endplates to the columns because of the limited wall thickness of the sections and the concern that the welding process would introduce considerable distortions into the sections. Instead, a Sikadur 31 FC Normal 2-part thixotropic epoxy resin was used to attach the endplates. The zinc coating was removed over a distance of 30 mm at the column ends to improve bond and the resin was poured into a mould around the column base up to a height of 20 mm. The epoxy resin was specified by the manufacturer to have a bond strength of 18 MPa and an elastic modulus of 6.6 GPa. Consequently, the height of 20 mm was sufficient to transfer a load of 350 kN in shear through the interface with the steel column, which well exceeded the column capacity for each specimen. In addition to providing a double row of connectors at each column end and manually filing the ends, the resin thus provided an extra means to ensure a uniform introduction of the load into all components.

3. Material Properties

The material properties of the test specimens were obtained by carrying out a series of tensile coupon tests. The coupons were cut from spare sections belonging to the same batch as those used in the test. Two flat coupons were taken along the centre line of the web of each type of channel section and along the centre line of the flat plate used in columns SC1. In addition, two corner coupons were cut from the web-flange junction of each type of channel section. Therefore, 18 coupons were tested in total. The dimensions of all coupons adhered to the specifications provided in [29]. In particular, all flat coupons had a nominal width of 12.5 mm and a gauge length of 50 mm. Each coupon was instrumented with an extensometer and one linear 5 mm strain gauge on each side of the coupon. After removing the zinc coating with an emery cloth, the width and thickness of each coupon were measured using a digital Vernier caliper with a precision of ±0.03 mm. All corner coupons had a nominal width of 6 mm. The coupons taken from the components of columns SC1 and SC2 had a gauge length of 25 mm. However, this gauge length was found to be too short to allow for an easy installation of the instrumentation onto the coupon, and therefore, the corner coupons taken from the components of columns SC3 and SC4 were subsequently cut with a gauge length of 50 mm. The corner coupons were tested in pairs in order to avoid eccentric tension. Two coupons extracted from the same type of channel were tested together, with a square bar placed in between the gripped ends, as shown in Figure 6. Each pair of corner coupons was instrumented with an extensometer. In addition, a 5 mm strain gauge was fitted to the outside of each coupon.

The cross-sectional area of the corner coupons was determined by photographing the end sections of the coupon using the reverse lens technique (Figure 7), importing the image into AutoCAD® software, superimposing the width of the coupon along the gauge length onto the picture and using the software features to automatically calculate the area of interest. The process was repeated with pictures taken from the opposite end of the coupon and agreement within 2-3% was obtained in all cases.

All coupons were tested following the specifications provided in the relevant European standard [29]. The tests were performed in a 300 kN Shimadzu AGS-X universal testing machine with a displacement rate of 1-2 mm/min. Each test was halted for 2 minutes at regular intervals, with the first pause imposed when yielding was first observed in the coupon. This allowed the load to settle down to 'static' values and eliminated strain rate effects. As an example, Figure 8 shows the ('static' and 'dynamic') stress-strain curves of one of the flat coupons and the pair of corner coupons taken from channel T12012. Stresses and strains shown in this figure are conventional 'engineering' values.

Table 6 lists the (static engineering) values of the 0.2 % proof stress ($\sigma_{0.2\%}$), the ultimate tensile strength (σ_u) and the elongation at fracture (ε_f) obtained for each coupon, as well as the average values over twin coupons. For the corner coupons extracted from sections T15414 and T7912 the elongation at fracture was based on a gauge length of 25 mm, while for the rest of corner coupons and all of the flat coupons this was based on a gauge length of 50 mm. It is important to note that although the 0.2 % proof stresses listed in the table are in some cases lower than the nominally specified values (i.e. 450 MPa for sections P20024, T15414 and T7912, and 260 MPa for sections T12012 and S11012), the values listed in the table correspond to the 'static' 0.2 % proof stresses, reduced to zero strain rate. The nominal values reported in practice are based on 'dynamic' values (with strain rates within the limits set by the standards).

4. Imperfection Measurements

Imperfections may have a significant influence on the stability of thin-walled structural members, particularly when coupled instabilities are involved [30,31] and the topic of imperfections in cold-formed steel structural members has previously received considerable investigative effort [32, 33]. For this reason, the imperfections of all test specimens were recorded before testing. The equipment used to carry out the measurements consisted of a steel table with a very high degree of flatness, a traverse system powered by electric motors travelling at a pre-determined constant speed and a laser displacement sensor. The flat table with dimensions of 1500×920 mm^2 was made of cast iron and was classified to be grade 3 according to [34], meaning that it provided a surface with a deviation from flatness of less than 0.06 mm. A traverse system consisting of an aluminium frame with a trolley, high-precision guiding bars and two electric motors was placed on top of the flat table, as illustrated in Figure 9. The frame had dimensions of 2400×600 mm^2 and rested on four adjustable supports. The two electric motors allowed movement of the laser sensor, which was attached to the trolley, along two orthogonal horizontal axes. Movement in the vertical direction was controlled manually by turning a crank handle located on the trolley (Figure 9). This permitted the laser sensor to be positioned within measuring range from the surface. The laser displacement sensor was a Keyence LK-G82 sensor with a beam spot diameter of 70 µm, a measurement range between 65 and 95 mm and an accuracy of ±0.0075 mm.

The imperfections were measured by moving the laser displacement sensor along different longitudinal lines on each face of the built-up column, as indicated by the red arrows in Figure 10 for each built-up geometry. The black arrows indicate measurements taken of the individual components before assembly, as access to them was restricted in the final configuration. Imperfection readings were considered positive in the direction away from the centroid of the column. For columns SC1 and SC2 the laser sensor was moved at a constant speed of 5 mm/s, while readings were taken with a sampling rate of 50 Hz, resulting in a reading every 0.1 mm. It was subsequently concluded that taking readings at such short intervals was not strictly necessary to obtain a representative imperfection profile. Therefore, the sampling rate was reduced to 5 Hz for columns SC3 and SC4, resulting in readings every 1 mm. Measurements of the nominally flat table, without a test specimen present, were used to correct for the out-of-straightness of the guiding bars along which the laser sensor was moved. Therefore, the accuracy of the measurements was determined by the flatness of the table and of the order of 0.06 mm.

The out-of-plane imperfection measurements were used to determine representative imperfections of the column components. For both the plain and the lipped channels, the imperfections of interest included the out-of-plane imperfections along the centre line of the web measured relative to the line connecting the corners (δ_{web}) and the out-of-plane imperfections along the flange edge measured relative to the web-flange junction δ_{flange} (where the 'flange edge' either indicates the free edge in the case of a plain channel or the flange-lip junction in the case of a lipped channel). For the lipped channels the out-of-plane imperfections along the centre line of the flange measured relative to the corners ($\delta_{flanges,L}$) were also considered. The flat plate components in columns SC1 were expected to buckle in a global flexural mode between connectors and for these sections the imperfections of interest (δ_{plate}) were computed as the average over the three measurement lines.

It is worth noting that the imperfections of the flanges of the channels in columns SC1 and the flanges of the inner channels in columns SC2 were not measured, since there was not enough space within the channels to place the laser sensor at an appropriate distance from the flanges. However, local buckling of these channel sections was expected to be mainly affected by the imperfections in the web, as this constituted the most slender part of the cross-section. Similarly, the imperfections of the lipped channels in columns SC3 and the imperfections of the plain channels in columns SC4 could not be measured after the specimens were assembled. Therefore, they were recorded prior to assembly. However, only the web imperfections of these channels were considered to be important due to the slenderness of the web and the geometric arrangement of the cross-section, where the flanges are connected to other components.

Figure 11 shows the out-of-plane imperfections recorded on a representative column with geometry SC1. The vertical dashed black lines indicate the locations of the connectors. The complete imperfection data of all specimens can be found in [28].

Table 7 lists, for each built-up geometry, the maximum and the average out-of-plane imperfections recorded on the individual components. The average value of δ_{flange} was computed assuming that δ_{flange} = 0 at the column ends. In other words, it was assumed that the flanges were perfectly orthogonal to the web at the column ends. However, to determine a maximum value of this imperfection it was deemed more representative to report the maximum value of δ_{flange} relative to the average value along the flange. The table shows that the maximum recorded imperfections were generally smaller than 1 mm in all components. Only channel T12012 in columns SC3 showed a maximum out-of-plane imperfection in the web larger than 1 mm. However, this relatively large imperfection was only recorded in one channel. The rest of the T12012 channels had maximum imperfections smaller than 0.57 mm. The recorded average imperfection was smaller than 0.36 mm in all components. It is worth pointing out that the maximum and average imperfections $\delta_{flange,L}$ in the S11012 lipped channels were smaller than the accuracy of the measuring frame and those values should therefore only be taken as an indication that the imperfections were very small.

5. Test Set up

All specimens were tested between fixed end supports in an ESH universal testing machine with 1000 kN capacity. To monitor whether the load was uniformly transmitted to each component of the column, a total of four columns –one of each geometry– were instrumented with strain gauges at mid-height. One strain gauge was placed on each individual component of the built-up column, along the centre line of the web of the channel or along the centre line of the flat plate. For each geometry, one of the columns with the least amount of connectors was chosen to be instrumented since the effects of uneven participation of the various components would have been most pronounced in these columns.

Two vertical potentiometers were placed underneath the end plate at the top of the specimen, one on each side of the column, to record the axial shortening of the specimens. The readings obtained from these two potentiometers were in close agreement for all specimens, indicating that fixed support conditions were successfully achieved and that no end rotation took place during the test. In addition, a number of potentiometers were placed in a horizontal position, typically divided over two cross-sections, to measure the out-of-plane deformations of the components and capture the onset of local buckling. Figure 12 illustrates the typical arrangement used for the columns of different geometry, indicating both the measuring locations within the cross-section and the vertical placement over the height of the specimens.

A consistent strain rate of 1.7×10^{-6} /s was applied to all specimens. This corresponded to a displacement rate of 0.112 mm/min for columns SC1, SC3 and SC4 (with a length of 1100 mm), and 0.082 mm/min for columns SC2 (with a length of 800 mm). Columns SC1 and SC2 were compressed over a range of 10 mm during the test, while columns SC3 and SC4 were compressed by up to 3.5 mm. This was sufficient to obtain the load-displacement graph until well past the peak load. Each test was halted for 3 minutes when approaching the peak load in order to determine the lower bound 'static' value of the load, independent of strain rate dependent effects.

The data acquisition system was controlled by a LabView script, which imposed a sampling rate of 1 Hz.

6. Test results

6.1. Strain gauge readings

Figure 13 shows a typical set of strain gauge readings over the course of the test for a column with geometry SC1. Compressive strains were taken as positive. The figure shows that the strains in the channel sections and the flat plate sections were in good agreement until buckling occurred at a load of approximately 60 kN. Below this load, the strain in the flat plate sections differed by at most 12 % from the column average, while this number was 11 % for the channel sections. The readings also show that the plates were typically subject to slightly lower strains than the channels. This can likely be attributed to the initial imperfections present in the plate sections, as well as to their low flexural stiffness. These imperfections caused out-of-plane deformations from an early load of approximately 10 kN, as evidenced by the potentiometer readings. Due to the presence of the channels the plates could only bend outwards, which introduced superimposed tensile stresses at the location of the strain gauges.

Similar general conclusions could be drawn for the other three geometries. Below the critical buckling load the load was observed to be evenly distributed over all components, with the maximum recorded difference in strain in the various components with respect to the column average ranging from 3% (geometry SC4) to 12% (geometry SC2). For geometry SC3 this value was 5%.

6.2. Observations of the deformations and failure modes

6.2.1 Columns SC1

All columns SC1 failed by interaction of global buckling of the flat plate components between connectors and local buckling of the channels. Each pair of twin columns showed the same initial buckled shape (Figure 14), although the eventual localization of the buckling pattern with the formation of a yield line pattern often occurred in different locations.

In columns SC1-2, which exhibited the largest connector spacing, the flat plate components buckled outwards in between connector points in a global-type flexural mode with a half-wavelength slightly beyond half the connector spacing (Figure 14a). However, the observation that the buckling deformations of the flat plates were localized in the central field of the column, with the adjacent fields remaining straight, was unanticipated. Seen the regularity of the buckling pattern in the adjacent channels, it is clear that a certain amount of bolt slip necessarily occurred in order to make this possible. The channel components maintained deformational compatibility with the unbuckled plate sections in the end fields by the flanges buckling inwards over the whole length of the column. The channels buckled with a half-wavelength equal to half the connector spacing. This can be explained by the fact that the signature curve of the unrestrained channels (Figure 15), obtained using CUFSM [27], displayed a fairly flat local buckling minimum for half-wavelengths between 140-200 mm, while the connector spacing of columns SC1-2 was 333 mm. The buckle half-wavelength of the flanges was slightly adjusted to be compatible with the buckle half-wavelength of the plates. In the post-peak range the channel deformations localized in the central field, while the buckling pattern largely disappeared in the end fields.

In columns SC1-3 the channel components buckled in a similar way, with the flanges bending inwards. The half-wavelength extended slightly beyond half the connector spacing, a fact which was particularly evident in the two central fields of the column. The flat plate components buckled outwards in two of the fields, with a half-wavelength sympathetic to the one observed in the channels, while they remained largely straight in the other two fields, prevented from buckling inwards by the presence of the channel webs. Similarly to columns SC1-2, the post-peak deformations localized in a field where the plates buckled outwards.

Columns SC1-5 featured a connector spacing of 167 mm, which was approximately equal to the natural local buckle half-wavelength of the channel components (Figure 15). Unlike what was observed in columns SC1-2 and SC1-3, the channels in columns SC1-5 buckled with a half-wavelength equal to the distance between the connectors, with the flanges alternatingly moving inwards and outwards in successive fields. The connector locations corresponded to the nodal lines of the buckling pattern, implying that they did not undergo any out-of-plane translations, but did accommodate the plate rotations. The flat plate components buckled in a shape which followed the flange tips in the fields where these moved outwards, while they remained straight in the fields where the flange tips moved inwards, prevented from maintaining complete conformity by the presence of the channel webs. This buckling pattern required some concentrated bending in the plate components around the connectors. Post-peak localization of the buckled shape occurred in the central field, where the plate components initially moved outwards.

It can be concluded from the above that the buckling pattern in columns SC1 was highly dependent on the connector spacing.

6.2.2 Columns SC2

Unlike in the columns SC1, where global buckling of one of the components in between connector points was prevalent, the buckling modes of the components of columns SC2 were all local. Columns SC2 aimed to study the interaction between the local buckling patterns in the inner and outer channels as a result of the presence of the connectors and contact between surfaces. Figure 16 illustrates the deformed shapes of the columns just before the peak load was reached.

In the columns with two rows of intermediate connectors (SC2-2) the buckle half-wavelength of the outer channels coincided with half the distance between the connectors. Due to the presence of the inner channels, the webs of the outer channels were forced to buckle outwards (away from the centre of the column). The buckled shape is shown in Figure 16a. It is noted that the natural half-wavelength of the outer channels in isolation was calculated to be 170 mm (Figure 17) using CUFSM [27], while the connector spacing was 233 mm. This stability analysis also revealed that for the outer channels, generating two half-waves between connectors is associated with a buckling stress which is lower than for any other pattern with an integer number of half-waves between connectors.

In columns SC2-4 the outer channels buckled with a half-wavelength equal to the distance between the connectors. This buckling pattern is shown in Figure 16b and can also be explained based on the results of the CUFSM buckling analysis of the unrestrained channel (Figure 17). The critical stress associated with a half-wavelength equal to the distance between connectors (L_{cr} = 140 mm) is 65 MPa, whereas generating buckles half that length (L_{cr} = 70 mm) would require a stress level of 112 MPa.

In columns SC2-6 the outer channels were observed to buckle with varying half-wavelength along the column. Along part of the specimen height the outer channels buckled with a half-wavelength very close to, but slightly beyond, the distance between connectors. However, this pattern switched to one in which the outer channels displayed a half-wave which spanned almost two fields over an intermediate connector, as illustrated in Figure 16c. This can be explained by the fact that these observed half-wavelengths are associated with a lower critical stress in the signature diagram than half-wavelengths equal to the connector spacing of 100 mm or twice that distance.

In all columns SC2 the inner channels buckled with a half-wavelength equal to half the distance between the connectors. Due to the presence of the outer channel webs, the flanges of the inner channels were forced to buckle towards the inside of the channels. This pattern occurred in all columns, despite the wide range of connector spacings, indicating a high degree of restraint on the inner channels.

6.2.3 Columns SC3

All columns SC3 failed by local buckling. Figure 18 shows the deformed shapes of the columns right before the peak load was reached, while a representative failure mechanism is shown in Figure 19 for column SC3-5b.

In all columns the lipped inner channels buckled with a half-wavelength of approximately 83 mm, corresponding to four and two half-waves between connectors for columns SC3-2 and SC3-5, respectively. In comparison, the natural local buckle half-wavelength of the unrestrained lipped channel is 90 mm, as shown by the signature diagram in Figure 20.

In columns SC3-2 the plain outer channels buckled with two to four half-waves between connectors. The cross-sections containing connectors thereby corresponded to the minima of the buckling pattern. In column SC3-2a the flanges of the outer channels followed the out-of-plane displacements of the webs of the inner channels almost perfectly. In its twin specimen SC3-2b, however, this was not the case, causing a more pronounced gap between the inner and outer channels, as is visible in Figure 18b. In this respect, it is also worth noting that the natural local buckle half-wavelength of the plain channels was 130 mm, which was associated with a critical stress of 79 MPa. Half-wave lengths of 83 mm (a quarter of the connector spacing) and 167 mm (half of the connector spacing) corresponded to buckling stresses of 91 MPa and 83 MPa, respectively.

A more regular buckling pattern was observed in the plain channels of the columns with five rows of intermediate connectors. In these columns, the web of the plain channels buckled with a half-wave length equal to half the distance between connectors (83 mm). This occurred despite the slightly larger buckling stress associated with this wavelength in comparison to a wavelength twice as long, and is indicative of the amount of restraint exerted by the inner onto the outer channels. In column SC3-5b the plain and lipped channels buckled in near complete sympathy, while in column SC3-5a the flanges of the plain channels (being less restrained by the connectors than the web) displayed a half-wavelength closer to their natural half-wavelength, resulting in the formation of some gaps between them and the webs of the lipped channels (Figure 18c).

6.2.4 Columns SC4

Columns SC4 failed predominantly by local buckling, with some minor participation of distortional buckling of the lipped channels. The potentiometer readings indicated that in columns SC4-2a, SC4-2b and SC4-5a, a minor amount of distortional buckling originated in one of the lipped channels just before the peak load was reached, while in column SC4-5b a minor amount of distortional buckling developed in both lipped channels simultaneously. Figure 21 illustrates the deformed shape of the columns shortly before the peak load was reached, while Figure 22 shows an example of the localized failure mechanism past the ultimate load.

In all SC4 columns the lipped channels first buckled in a local mode with a half-wavelength of approximately 83 mm, corresponding to a quarter of the connector spacing and half of the connector spacing in specimens SC4-2 and SC4-5, respectively. As the webs of the plain channels prevented the webs of the lipped channels from buckling towards the inside of the column, the flanges of the lipped channels were forced to buckle inwards.

6.3. Critical buckling stresses

An estimate of the buckling stress of the critical components of the built-up specimens was derived from the potentiometers readings by assuming that, up to the point of first buckling, the load was uniformly distributed over all components, and that the initial post-buckling out of plane displacements follow a parabolic trend, as shown in Figure 23 for column SC2-2a. After fitting a parabola to these initial displacements, the buckling load followed from the intersection of this parabola with the vertical axis. Further details and examples, as well as all potentiometer readings as a function of the load applied to the column, can be found in [28]. For those columns instrumented with strain gauges these buckling stresses were in good agreement with the values obtained from the strain gauge readings using the strain reversal method [35].

The experimental buckling stresses were compared to theoretical buckling stresses, calculated based on the measured cross-sectional dimensions (averaged over the two components in the cross-section) and using the Young's modulus obtained from the flat tensile coupons (Tables 8-11). The theoretical buckling stresses were obtained while considering the individual components in isolation, without any interaction with the rest of the cross-section, and adopting the buckle half-wavelength observed during the test. For the plain and lipped channel sections the theoretical critical buckling stresses were obtained using the CUFSM 4.05 software [27], while for the plate components in columns SC1 the critical buckling stress was determined using Euler's equation:

$$\sigma_{cr} = \frac{\pi^2 E t^2}{12 L_p^2} \tag{1}$$

In the above Eq. (1), E is the Young's modulus, t is the averaged measured thickness of the two plate sections in the column and L_p is the buckle half-wave length (effective length). Eq. (1) was evaluated using two different values of L_p. An upper bound for σ_{cr} was established by taking L_p equal to half the connector spacing, while a lower bound was obtained by assuming L_p to be equal to the connector spacing (Table 8).

Table 8 shows that the experimental buckling stresses of the flat plate components were intermediate between the theoretical lower and upper bounds. This agrees with the experimentally observed buckled shape, as described in Section 6.2.1. An estimate of the local buckling stress of the channels in the SC1 columns could also be derived from the experiment by assuming that, due to the lack of post-buckling capacity in the global flexural mode, any increase in load after buckling of the flat plate took place was entirely resisted by the channels. This approach demonstrated that the channels buckled at a stress very close to the theoretically predicted value. This suggests that the channels were not significantly affected by any restraint provided by the plates, which buckled either before or simultaneously with the channels.

Table 9 lists the theoretically predicted buckling stresses of the inner and outer channels of the SC2 columns . Only the buckling stresses of the outer channels could be experimentally determined (by dividing the load at which their buckling was observed over the gross cross-sectional area), since the load sharing between the outer channels in their post-buckled state and the inner channels is a non-trivial problem. In some columns the two outer channels buckled at slightly different loads, as shown in Figure 23, and in this case both values are reported in Table 9. The buckling stresses of the outer channels obtained from the test were generally slightly larger than the predicted values, with the difference increasing as the connector spacing was reduced. For columns SC2-6 the difference became quite substantial, with the buckling stresses obtained from the test being around 35 % larger than the theoretical ones. This indicates a more significant amount of restraint exerted by the inner channels onto the outer channels as the connector spacing decreased.

The theoretical and experimental critical buckling stresses of the components of the SC3 columns are listed in Table 10. The plain and the lipped channels buckled approximately at the same time in all columns. In those columns in which the plain channels were seen to buckle in a mixed pattern with two different buckle half-wavelengths, the stresses associated with both half-wavelengths are included in the table. The channels were experimentally observed to buckle at a stress level of approximately 103 MPa. This stress is very close to the theoretically predicted buckling stress of the lipped channels, while it is around 40 % higher than the buckling stress predicted for the plain channels. This indicates that the plain channels substantially benefited from the restraint provided by the lipped channels.

Table 11 lists the theoretical and experimental buckling stresses of the different components of the SC4 columns. In columns SC4-2, the plain channels buckled before the lipped channels, while in columns SC4-5 all components buckled at approximately the same time. This allowed the experimental buckling stresses of the lipped channels of columns SC4-5, as well as the experimental buckling stresses of the plain channels of all columns to be determined. Table 11 shows that the plain channels buckled at an increased stress level compared to the theoretical predictions. This was due to the restraint exerted by the lipped channels, which forced the flanges of the plain channels to buckle inwards. The lipped channels, on the other hand, buckled at stresses close to, or slightly below, the theoretically predicted values.

6.4. Ultimate load

Figure 24a-d plot the (static) load vs. axial displacement curves of all columns with geometries SC1, SC2, SC3 and SC4, respectively. It is worth pointing out the marked decrease in the stiffness of columns SC1 after first buckling of the plate components took place, compared to the more gradual decrease in stiffness observed in the columns with geometries SC2, SC3 and SC4. This can be explained by the fact that the plates contributed 57 % to the total cross-sectional area of the SC1 columns, while after buckling in a global flexural mode, these plates were unable to contribute in resisting a further increase in load.

The ultimate loads obtained for all columns with geometries SC1, SC2, SC3 and SC4 are listed in Table 12. The average value for each set of twin columns is also provided.

Table 12 shows that, regarding columns SC1, the difference in the ultimate load achieved in twin specimens was 9 % for columns SC1-2, 4 % for columns SC1-3 and 7 % for columns SC1-5. The tests also showed a moderate increase in ultimate load as the spacing between connectors was reduced. More specifically, halving the connector spacing from 333 mm to 167 mm produced an increase in the average ultimate load of 11 %.

In columns SC2 good agreement was again obtained between the results of twin specimens. The difference in ultimate load was 6 % for columns SC2-2, 2 % for columns SC2-4 and 5 % for columns SC2-6. In this case the tests showed that reducing the spacing between connectors did not necessarily result in a noticeable increase in ultimate load. The columns with a connector spacing of 140 mm (columns SC2-4) showed similar ultimate loads compared to the columns with connectors spaced every 100 mm (columns SC2-6). However, the largest connector spacing (233 mm) did result in a slightly lower ultimate load, which was on average 9 % below that of the SC2-6 columns.

The difference in ultimate load between twin specimens of the SC3 columns was 3 % for columns SC3-5 and just 1 % for columns SC3-2. The results also show that halving the connector spacing from 333 mm to 167 mm only resulted in a negligible increase in ultimate capacity of 2 %.

With respect to columns SC4, the difference in ultimate load between twin specimens was 3 % for columns SC4-5 and 0.7 % for columns SC4-2. In this case, reducing the connector spacing actually resulted in a slight reduction in the ultimate capacity. More specifically, halving the connector spacing from 333 mm to 167 mm caused a reduction in the ultimate capacity of 6 %. This difference is quite marginal and might be due to the statistical variation of the relevant parameters (imperfections, geometry, material properties, etc.).

7. Conclusions

An experimental program was carried out consisting of 20 built-up thin-walled stub columns with four different cross-sectional geometries. The cross-sections were assembled from flat plates, plain channels and lipped channels with nominal thicknesses ranging from 1.2 mm to 2.4 mm. Two of the cross-sectional geometries (SC1 and SC2) were assembled using M6 bolts, while the other two (SC3 and SC4) were assembled using M5.5 self-drilling sheet metal screws. The connector spacing was varied among specimens of the same cross-sectional geometry. The experimental investigation included tensile coupon tests to determine the material properties of the flat portions and the corner regions of the different components. Accurate measurements of the out-of-plane geometric imperfections of the specimens were also carried out using a laser sensor. The columns were compressed between fixed supports in a displacement controlled regime. Strain gauge readings obtained from a select number of specimens confirmed a uniform introduction of the load into all components of the cross-sections. This was achieved thanks to hand-filing the end sections, placing a double row of connectors at the specimen ends and epoxy-gluing the end plates to the specimens.

Substantially different buckling patterns were generally observed in columns with the same cross-sectional geometry, but different connector spacing. The observations of the deformed column shapes also indicated that the buckling patterns of the individual components within the columns were subject to considerable restraint. This restraint manifested itself in two different ways: (1) a change in the natural local buckle half-wavelength to accommodate the presence of the connectors, and (2) contact between adjacent surfaces forcing the buckling out-of-plane displacements to occur exclusively in a certain direction.

Out of all the possible buckling patterns compatible with the constraints imposed by the connectors and contact between components, the one with the lowest buckling stress materialized. This resulted in some cases in a buckling pattern with a varying half-wavelength along the member, as was observed in the outer channels of columns SC2-6, or in a buckling pattern localized in one field, as seen in the plate sections of columns SC1-

2 and SC1-3. The latter was only possible after some slip occurred between the components at the connector points.

The experimentally derived buckling stresses were compared to theoretical predictions which considered the individual components in isolation, without any interaction with the rest of the cross-section, but used the experimentally observed wave-lengths. It was concluded that the buckling stress of the most slender components was increased by up to 44 % as a result of the restraint provided by the remainder of the cross-section. The amount of restraint was dependent on the connector spacing.

In terms of the cross-sectional capacity, columns SC1 exhibited a modest increase in ultimate strength of around 11 % when halving the connector spacing. This gain was mainly a result of the increase in the flexural buckling capacity of the plate sections in between connectors. When the critical buckling modes of the individual components were all local, the difference was even smaller. Only the SC2-2 columns showed around 11 % less capacity than the SC2-4 and SC2-6 columns, which had similar capacities. For columns SC3 and SC4 the effect of the connector spacing was negligible or non-existent.

Acknowledgement

The authors are grateful for the financial support provided by the EPSRC through grant EP/M011976/1.

References

[1] Schafer BW. Cold-formed steel structures around the world. Steel Construction 2011; 4; 141–149.

[2] Zhang X, Rasmussen K. Tests of cold-formed steel portal frames with slender sections. Steel Construction 2014; 7; 199–203.

[3] AISI (2016), North American Specification for the Design of Cold-Formed Steel Structural Members.

[4] CEN (2006), Eurocode 3 — Design of steel structures — Part 1-3: General rules — Supplementary rules for cold-formed members and sheeting. British Standard Institution.

[5] Stone TA, LaBoube RA. Behavior of cold-formed steel built-up I-sections. Thin-Walled Structures 2005; 43; 1805-1817.

[6] Fratamico DC, Torabian S, Zhao X, Rasmussen KJR, Schafer BW. Experiments on the global buckling and collapse of built-up cold-formed steel columns. Journal of Constructional Steel Research 2018; 144; 65–80.

[7] Lu Y, Zhou T, Li W, Wu H. Experimental investigation and a novel direct strength method for cold-formed built-up I-section columns. Thin-Walled Structures 2017; 112; 125–139.

[8] Zhang J-H, Young B. Compression tests of cold-formed steel I-shaped open sections with edge and web stiffeners. Thin-Walled Structures 2012; 52; 1–11.

[9] Abbasi M, Khezri M, Rasmussen KJR. On extending the direct strength method to the design of cold - formed steel built - up columns. EUROSTEEL 2017. Copenhagen. Denmark.

[10] Craveiro HD, Paulo J, Rodrigues C, Laím L. Buckling resistance of axially loaded cold-formed steel columns. Thin-Walled Structures 2016; 106; 358–375.

[11] Liao F, Wu H, Wang R, Zhou T. Compression test and analysis of multi-limbs built-up cold-formed steel stub columns. Journal of Constructional Steel Research 2017; 128; 405–415.

[12] Whittle J, Ramseyer C. Buckling capacities of axially loaded, cold-formed, built-up C-channels. Thin-Walled Structures 2009; 47; 190–201.

[13] Reyes W, Guzmán A. Evaluation of the slenderness ratio in built-up cold-formed box sections. Journal of Constructional Steel Research 2011; 67; 929–935.

[14] Young B, Chen J. Design of Cold-Formed Steel Built-Up Closed Sections with Intermediate Stiffeners. Journal of Structural Engineering 2008; 134; 727–737.

[15] Zhang JH, Young B. Experimental investigation of cold-formed steel built-up closed section columns with web stiffeners. Journal of Constructional Steel Research 2018; 147; 380–392.

[16] Li Y, Li Y, Wang S, Shen Z. Ultimate load-carrying capacity of cold-formed thin-walled columns with built-up box and I section under axial compression. Thin-Walled Structures 2014; 79; 202–217.

[17] Georgieva I, Schueremans L, Roeck G, Pyl L. Experimental Investigation of the Deformation of Built-up Members of Cold-formed Steel Profiles. Applied Mechanics and Materials 2011; 70; 416–421.

[18] Georgieva I, Schueremans L, Pyl L. Composed columns from cold-formed steel Z-profiles: Experiments and code-based predictions of the overall compression capacity. Engineering Structures 2012; 37; 125–134.

[19] Georgieva I, Schueremans L, Pyl L, Vandewalle L. Experimental investigation of built-up double-Z members in bending and compression. Thin-Walled Structures 2012; 53; 48–57.

[20] Georgieva I, Schueremans L, Pyl L, Vandewalle L. Numerical study of built-up double-Z members in bending and compression. Thin-Walled Structures 2012; 60; 85–97.

[21] Piyawat K, Ramseyer C, Kang TH. Development of an Axial Load Capacity Equation for Doubly Symmetric Built-Up Cold-Formed Sections. Journal of Structural Engineering 2013; 139; 1–13.

[22] Brueggen B, Ramseyer C. Capacity of built-up cold-formed steel axial compression members. Proceeding of the Annual Stability Conference 2005. Missouri. pp. 89–103.

[23] Piyawat K, Ramseyer C, Kang TH. Nonlinear buckling of built-up cold-formed sections. Journal of Theoretical and Applied Multiscale Mechanics 2011; 2; 145–164.

[24] Meza FJ, Becque J, Hajirasouliha I. Forthcoming. Experimental study of cold-formed steel built-up beams. Journal of Structural Engineering. DOI: 10.1061/(ASCE)ST.1943-541X.0002677.

[25] Meza FJ, Becque J, Hajirasouliha I. Experimental study of cold-formed steel built-up columns. Thin-Walled Structures 2020;149.

[26] Ziemian RD. Appendix B - Technical Memoranda of Structural Stability Research Council 2010.

[27] Schafer BW. Buckling analysis of cold-formed steel members using CUFSM: conventional and constrained finite strip methods. 18th International Specialty Conference on Cold-Formed Steel Structures 2006. Orlando. Florida.

[28] Meza FJ. The Behaviour of Cold-Formed Steel Built-up Structural Members. PhD thesis. The University of Sheffield 2018. UK.

[29] BS EN ISO 6892-1:2009 - Metallic materials — Tensile testing — Part 1 : Method of test at ambient temperature. British Standard Institution. 2009.

[30] Van der Neut A. The interaction of local buckling and column failure of thin-walled compression members. Proceedings 12th International Congress of Applied Mechanics 1969; 389–399.

[31] Becque J. Local-overall interaction buckling of inelastic columns: A numerical study of the inelastic Van der Neut column. Thin-Walled Structures 2014; 81; 101–107.

[32] Schafer BW, Pekoz T. Computational modelling of cold-formed steel: characterizing geometric imperfections and residual stresses. Journal of Constructional Steel Research 1998; 47; 193-210.

[33] Zeinoddini VM, Schafer BW. Simulation of geometric imperfections in cold-formed steel members using spectral representation approach 2012;60;105-117.

[34] BS 817:2008 - Specification for surface plates. 2008.

[35] Venkataramaiah KR, Roorda J. Analysis of Local Plate Buckling Experimental Data. Sixth International Specialty Conference on Cold-Formed Steel Structures 1982. St. Louis. Missouri.

Table 1: Nominal dimensions of the component sections

Column	section	*h* (mm)	*b* (mm)	*l* (mm)	*t* (mm)	r_{int} (mm)
SC1	T15414	154	54	-	1.4	2.8
	P20024	200	-	-	2.4	-
SC2	T15414	154	54	-	1.4	2.8
	T7912	79	36	-	1.2	2.4
SC3/SC4	T12012	120	40	-	1.2	2.4
	S11012	110	50	10	1.2	2.4

Table 2: Measured dimensions of built-up columns 1

Column	Channel				Plate		
	section	*h* (mm)	*b* (mm)	*t* (mm)	section	*h* (mm)	*t* (mm)
SC1-2a	T15414-1	153.96	53.90	1.452	P20024-1	199.83	2.476
	T15414-2	154.19	53.60	1.440	P20024-2	199.73	2.466
SC1-2b	T15414-3	154.09	53.83	1.444	P20024-3	199.67	2.474
	T15414-4	154.09	53.43	1.435	P20024-4	199.83	2.472
SC1-3a	T15414-5	154.19	53.73	1.441	P20024-5	199.53	2.493
	T15414-6	154.06	53.65	1.441	P20024-6	199.27	2.486
SC1-3b	T15414-7	154.13	53.41	1.429	P20024-7	199.43	2.482
	T15414-8	154.06	53.73	1.445	P20024-8	200.40	2.481
SC1-5a	T15414-9	154.13	53.58	1.437	P20024-9	200.10	2.478
	T15414-10	154.13	53.61	1.429	P20024-10	199.47	2.477
SC1-5b	T15414-11	154.09	53.35	1.417	P20024-11	198.93	2.472
	T15414-12	154.19	53.60	1.425	P20024-12	198.73	2.487
Average		154.11	53.62	1.436		199.58	2.479
St. Dev.		0.067	0.166	0.010		0.465	0.008

Table 3: Measured dimensions of built-up columns 2

Column	Channel				Channel			
	section	*h* (mm)	*b* (mm)	*t* (mm)	section	*h* (mm)	*b* (mm)	*t* (mm)
SC2-2a	T15414-1	154.03	53.43	1.426	T7912-1	78.93	36.26	1.147
	T15414-2	154.06	53.28	1.416	T7912-2	78.99	36.25	1.172
SC2-2b	T15414-3	153.96	53.46	1.428	T7912-3	78.83	36.40	1.142
	T15414-4	153.96	53.40	1.407	T7912-4	79.13	36.30	1.176
SC2-4a	T15414-5	154.03	53.58	1.43	T7912-5	79.16	36.40	1.145
	T15414-6	153.96	53.26	1.438	T7912-6	79.09	36.46	1.169
SC2-4b	T15414-7	154.03	53.70	1.434	T7912-7	79.06	36.50	1.128
	T15414-8	154.13	53.51	1.436	T7912-8	79.13	36.46	1.166
SC2-6a	T15414-9	154.03	53.51	1.422	T7912-9	79.03	36.51	1.143
	T15414-10	154.29	53.35	1.417	T7912-10	79.06	36.41	1.172
SC2-6b	T15414-11	154.16	53.73	1.433	T7912-11	79.03	36.16	1.141
	T15414-12	154.23	53.68	1.431	T7912-12	78.99	36.30	1.171
Average		154.07	53.49	1.427		79.04	36.37	1.156
St. Dev.		0.108	0.158	0.009		0.093	0.111	0.016

Table 4: Measured dimensions of built-up columns 3

	Channel					Channel			
Column	section	*h* (mm)	*b* (mm)	*t* (mm)	section	*h* (mm)	*b* (mm)	*l* (mm)	*t* (mm)
SC3-2a	T12012-1	119.61	39.97	1.117	S11012-1	110.46	49.83	9.83	1.109
	T12012-2	119.97	40.01	1.090	S11012-2	111.07	49.93	9.87	1.095
SC3-2b	T12012-3	119.82	40.07	1.102	S11012-3	110.75	49.79	9.83	1.107
	T12012-4	119.84	39.99	1.097	S11012-4	110.91	49.92	9.88	1.090
SC3-5a	T12012-5	119.96	40.03	1.118	S11012-5	110.80	49.97	9.79	1.098
	T12012-6	119.81	40.01	1.127	S11012-6	110.44	49.93	9.89	1.119
SC3-5b	T12012-7	119.59	39.99	1.124	S11012-7	110.07	49.90	9.87	1.120
	T12012-8	119.72	39.95	1.095	S11012-8	110.85	49.82	9.85	1.098
Average		119.79	40.00	1.109		110.67	49.88	9.85	1.104
St. Dev.		0.144	0.035	0.014		0.325	0.064	0.033	0.011

Table 5: Measured dimensions of built-up columns 4

	Channel					Channel			
Column	section	*h* (mm)	*b* (mm)	*t* (mm)	section	*h* (mm)	*b* (mm)	*l* (mm)	*t* (mm)
SC4-2a	T12012-9	119.70	39.94	1.101	S11012-9	111.07	49.98	9.76	1.094
	T12012-10	119.90	39.98	1.089	S11012-10	111.13	49.91	9.86	1.088
SC4-2b	T12012-11	119.90	39.97	1.085	S11012-11	111.08	49.88	9.83	1.086
	T12012-12	119.83	39.97	1.096	S11012-12	110.89	49.83	9.87	1.097
SC4-5a	T12012-13	119.71	40.01	1.096	S11012-13	110.15	49.89	9.88	1.120
	T12012-14	119.89	39.98	1.096	S11012-14	111.11	49.86	9.88	1.103
SC4-5b	T12012-15	119.77	40.00	1.118	S11012-15	110.79	49.82	9.78	1.115
	T12012-16	119.67	40.05	1.120	S11012-16	110.87	49.92	9.84	1.092
Average		119.80	39.99	1.100		110.89	49.89	9.84	1.099
St. Dev.		0.097	0.034	0.013		0.325	0.050	0.046	0.012

Table 6: Material properties of tensile coupons

Type	Section	Coupon	E (GPa)		$\sigma_{0.2\%}$ (MPa)		σ_u (MPa)		ε_f (%)	
			Ind.	Avg.	Ind.	Avg.	Ind.	Avg.	Ind.	Avg.
Flat	P20024	a	203	197	425	428	464	465	-	17
Flat	P20024	b	191		430		466		17	
Flat	T15414	a	213	214	617	604	656	647	11	12
Flat	T15414	b	215		591		637		13	
Flat	T7912	a	200	198	430	411	480	483	14	15
Flat	T7912	b	195		391		485		16	
Flat	T12012	a	190	192	244	242	319	320	30	31
Flat	T12012	b	194		240		321		31	
Flat	S11012	a	197	198	275	277	356	357	28	28
Flat	S11012	b	198		279		357		27	
Corner	T15414	a	214	222	-	604	-	676	-	11
Corner	T15414	b	230		-		-		-	
Corner	T7912	a	192	199	-	462	-	522	-	18
Corner	T7912	b	206		-		-		-	
Corner	T12012	a	237	235		309		353		16
Corner	T12012	b	234							
Corner	S11012	a	276	258		344		384		12
Corner	S11012	b	239							

Table 7: Maximum and average imperfection measurements

Specimen	Section	Imperfection (mm)		
			Max.	Avg.
SC1	P20024	δ_{plate}	0.60	0.21
	T15414	δ_{web}	0.64	0.13
SC2	T7912	δ_{web}	0.36	0.14
	T15414	δ_{web}	0.69	0.15
		δ_{flange}	0.47	0.19
SC3	T12012	δ_{web}	1.04	0.20
		δ_{flange}	0.58	0.30
	S11012*	δ_{web}	0.49	0.08
SC4	S11012	δ_{web}	0.39	0.09
		δ_{flange}	0.57	0.36
		$\delta_{flange,L}$	0.06	0.01
	T12012*	δ_{web}	0.26	0.11
*Imperfections recorded before the sections were assembled				

Table 8: Buckling stresses of the components of columns SC 1

Column	Theoretical buckling stress (MPa)			Buckling stress from test (MPa)	
	Channel	Plate		Channel	Plate
		Lower	Upper		
SC1-2a	71	9	35	65	28
SC1-2b	71	9	36	72	19
SC1-3a	76	16	64	70	46
SC1-3b	75	16	64	69	45
SC1-5a	70	36	144	69	69
SC1-5b	69	36	145	67	67

Table 9: Buckling stresses of the components of columns SC2

Column	Theoretical buckling stress (MPa)		Buckling stress from test (MPa)	
	Inner Channel	Outer Channel	Inner Channel	Outer Channel
SC2-2a	132	76	-	77-95
SC2-2b	132	76	-	79
SC2-4a	140	72	-	69-86
SC2-4b	139	72	-	86
SC2-6a	180	70-84	-	105
SC2-6b	181	71-86	-	105
Note: "-" indicates no estimation of the buckling stress was made as the component was not the first one to buckle.				

Table 10: Buckling stresses of the components of columns SC3

Column	Theoretical buckling stress (MPa)		Buckling stress from test (MPa)	
	Plain Channel	Lipped Channel	Plain Channel	Lipped Channel
SC3-2a	67-74	103	103	103
SC3-2b	67-74	102	84-96	96
SC3-5a	70-77	104	-	96-117
SC3-5b	75	104	108	108

Note: “-“indicates no estimation of the buckling stress was made as the component was not the first one to buckle

Table 11: Buckling stresses of the components of columns SC4

Column	Theoretical buckling stress (MPa)		Buckling stress from test (MPa)	
	Plain Channel	Lipped Channel	Plain Channel	Lipped Channel
SC4-2a	66-73	100	87	-
SC4-2b	66-72	100	88	-
SC4-5a	66-73	105	73-91	91
SC4-5b	69-76	103	93-104	104

Note: “-“ indicates no estimation of the buckling stress was made as the component was not the first one to buckle

Table 12: Ultimate loads

Column	Ultimate load (kN)	Average ultimate load (kN)
SC1-2a	183.97	176.07
SC1-2b	168.17	
SC1-3a	183.01	179.44
SC1-3b	175.86	
SC1-5a	201.72	195.11
SC1-5b	188.50	
SC2-2a	213.32	206.83
SC2-2b	200.34	
SC2-4a	238.00	235.70
SC2-4b	233.39	
SC2-6a	220.54	226.58
SC2-6b	232.62	
SC3-2a	139.30	138.92
SC3-2b	138.53	
SC3-5a	138.77	141.08
SC3-5b	143.40	
SC4-2a	148.09	147.56
SC4-2b	147.03	
SC4-5a	141.23	139.49
SC4-5b	137.74	

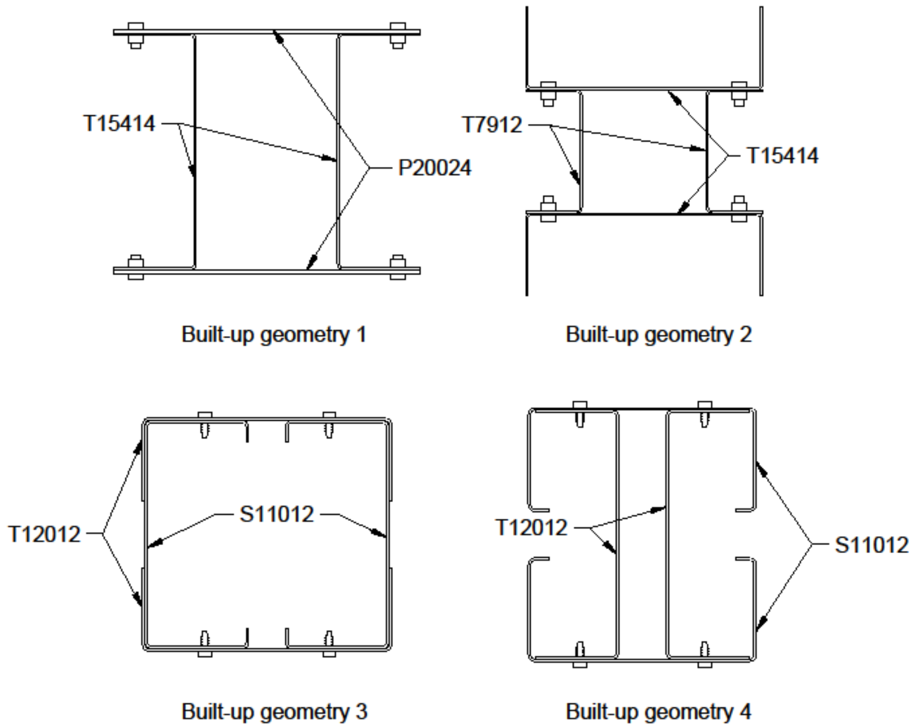

Figure 1: Built-up cross sections

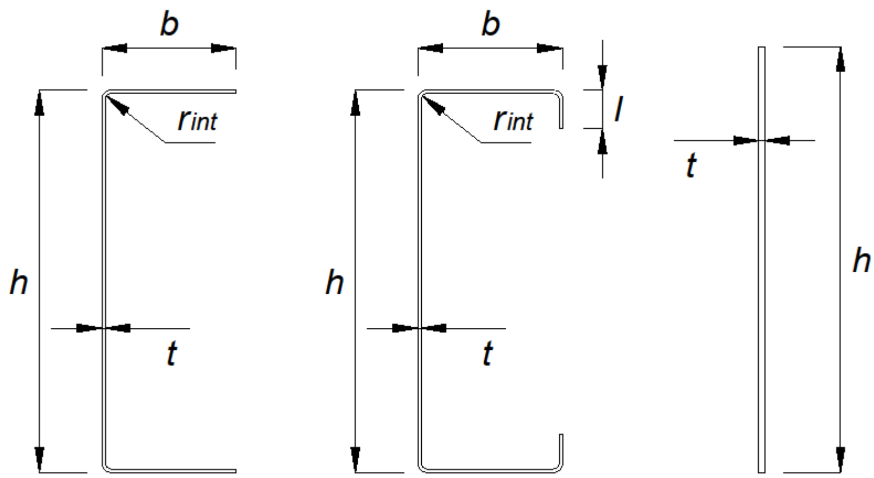

Figure 2: Nomenclature used to refer to the dimensions of the component sections

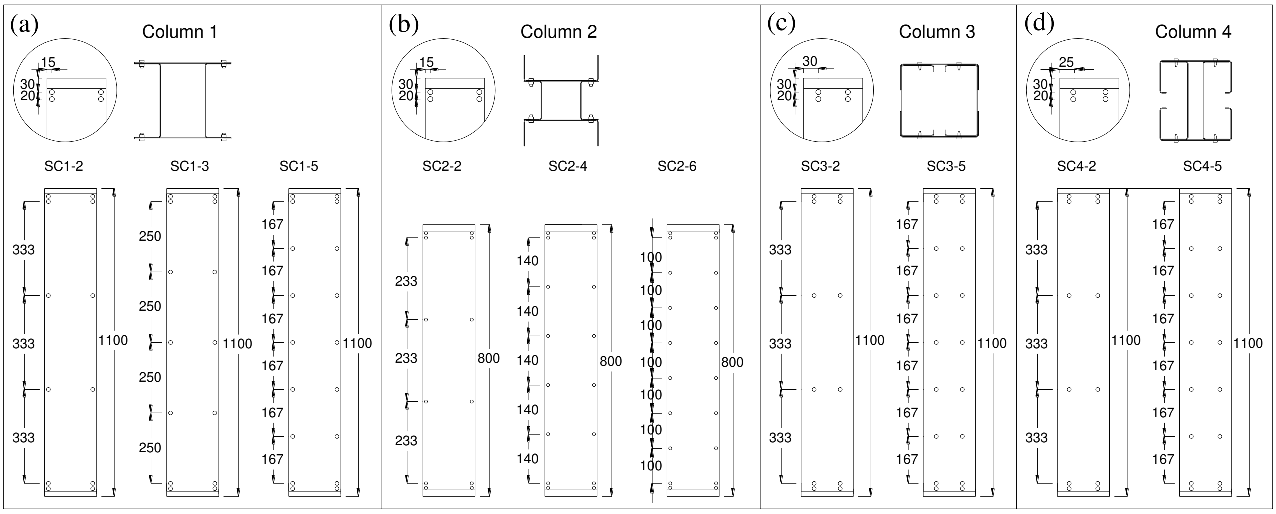

Figure 3: Location of connectors in: a) columns SC1; b) columns SC2; c) columns SC3 and d) columns SC4

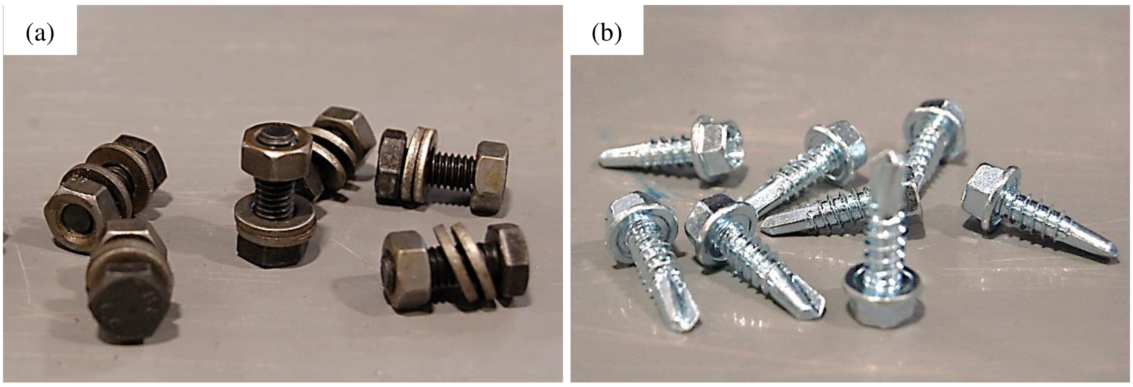

Figure 4: a) M6 bolts, b) M5.5 self-drilling screws

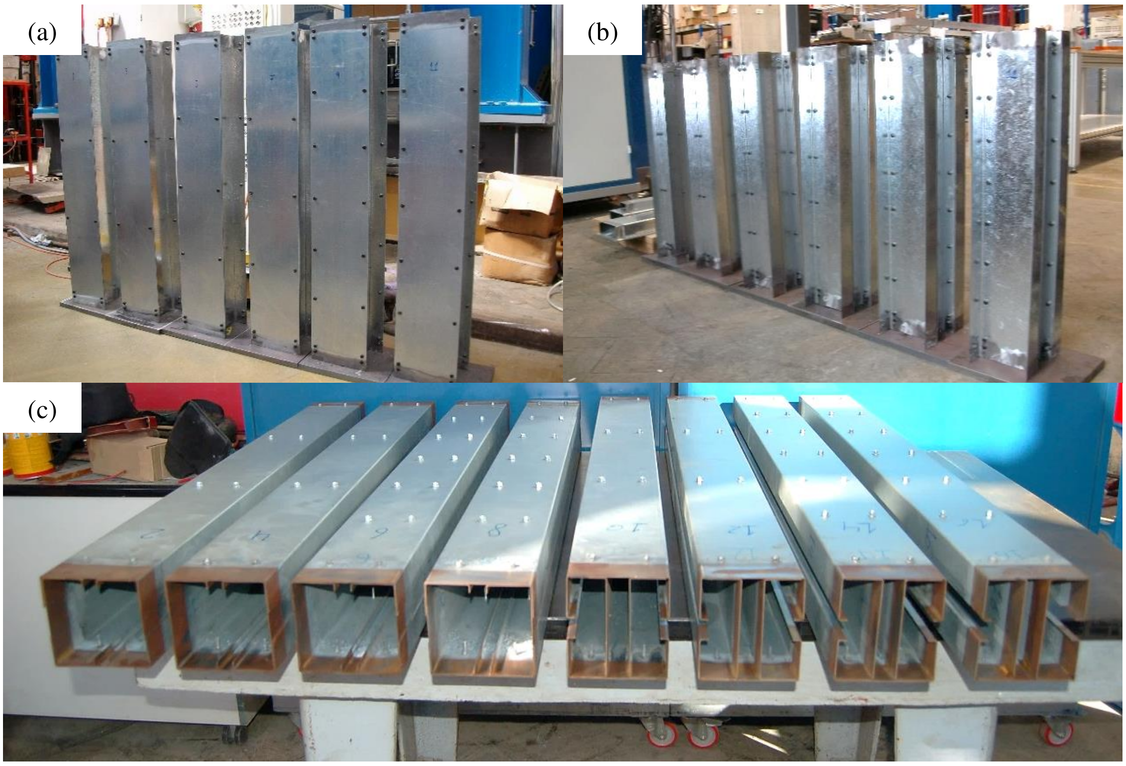

Figure 5: Built-up columns after assembly: a) columns SC1, b) columns SC2, and c) columns SC3 and SC4

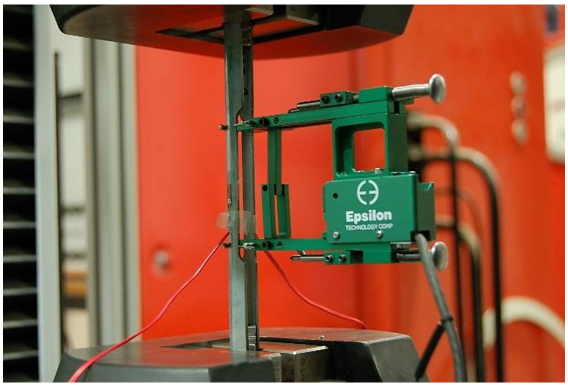

Figure 6: Corner coupons test set-up

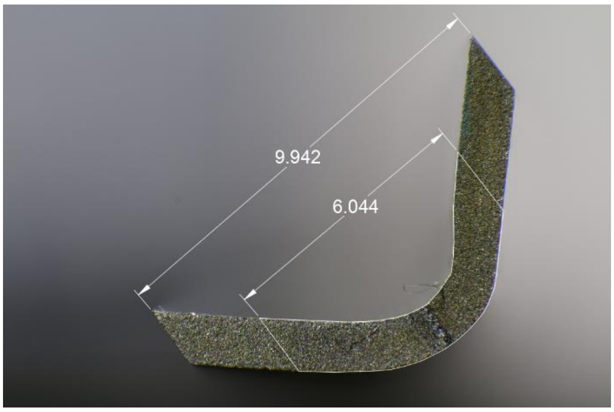

Figure 7: Photograph of the cross-section of corner coupon T10412a

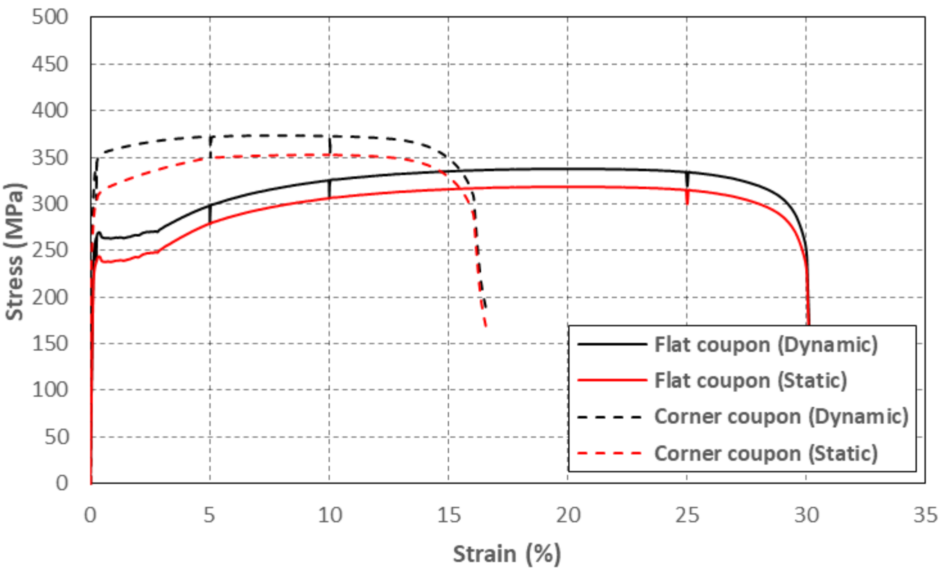

Figure 8: T12012: Flat and corner coupon test results

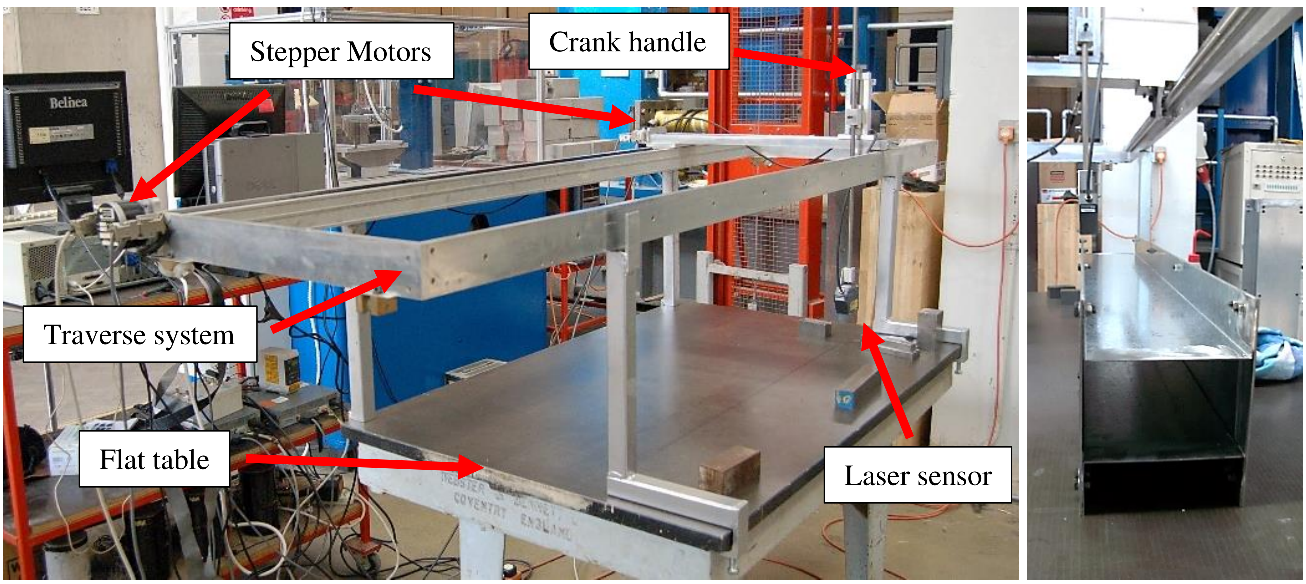

Figure 9: Imperfection measuring set-up

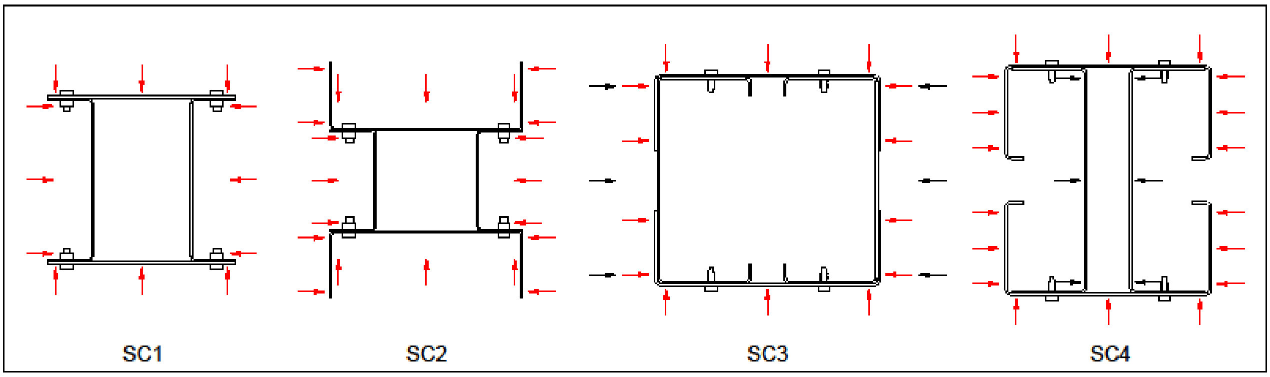

Figure 10: Location of the imperfection measurements

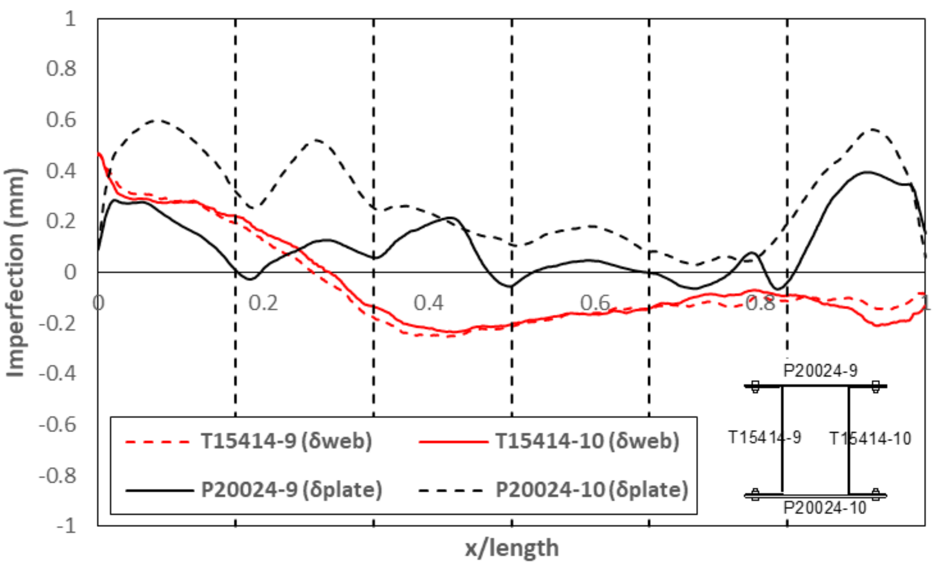

Figure 11: Out-of-plane imperfections in column SC1-5a

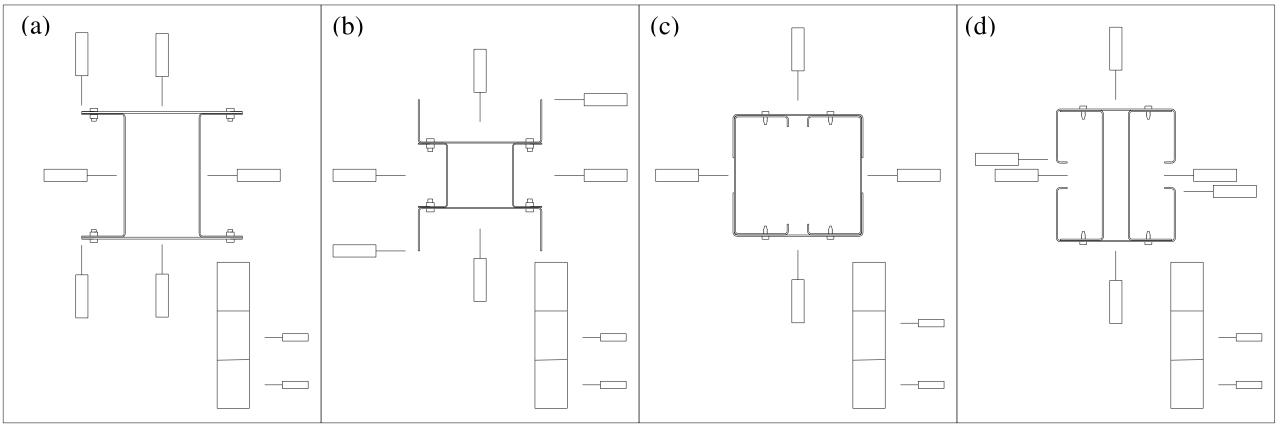

Figure 12: Potentiometer arrangement for: a) SC1; b) SC2; c) SC3 and d) SC4

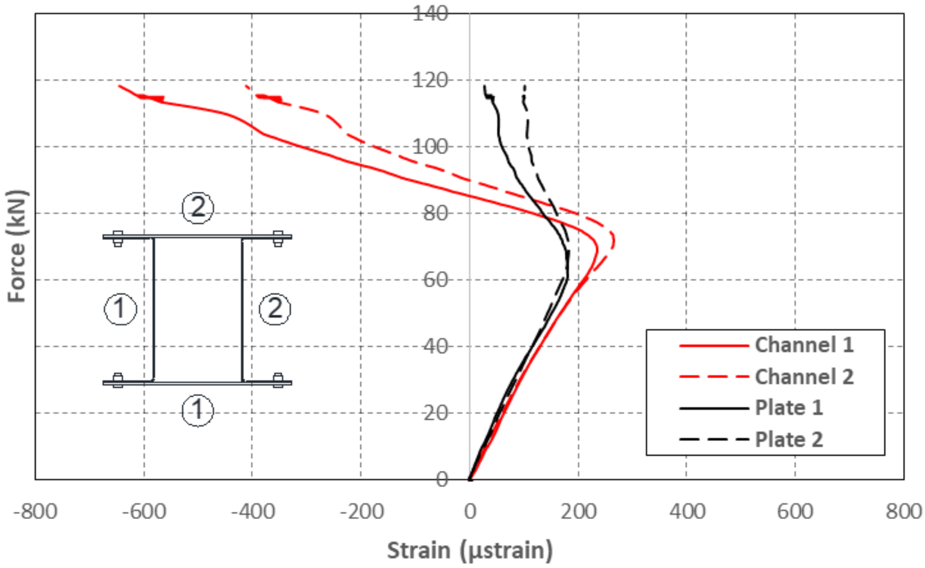

Figure 13: Axial load vs compressive strain in column SC1-2a

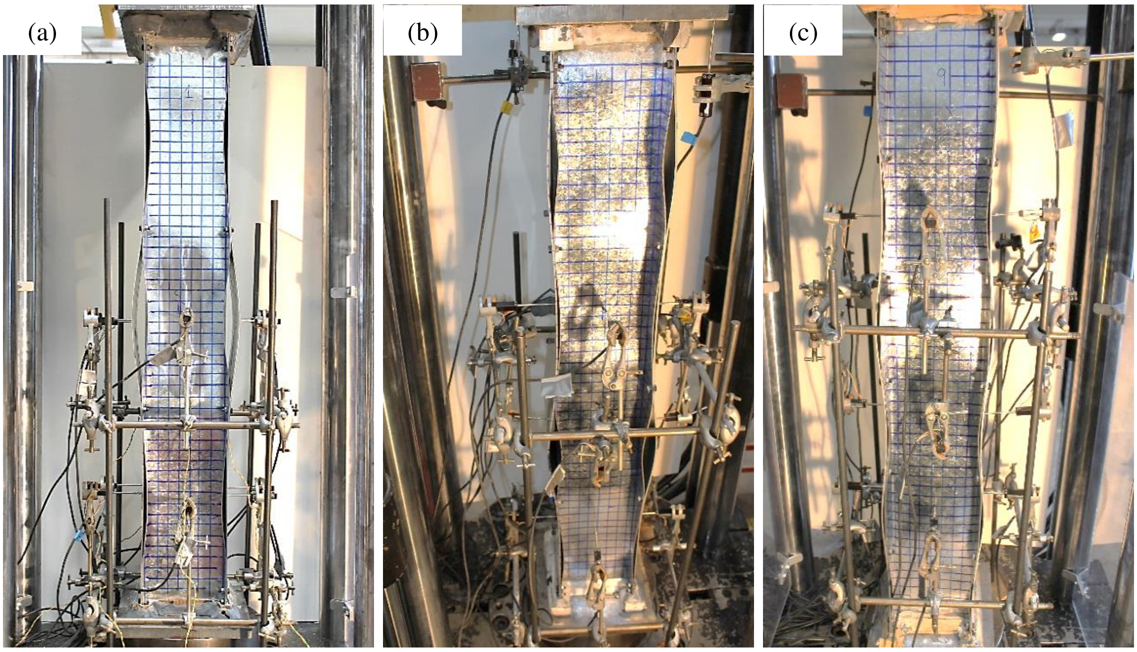

Figure 14: Deformed shape approaching ultimate load in a) SC1-2a, b) SC1-3a, c) SC1-5a

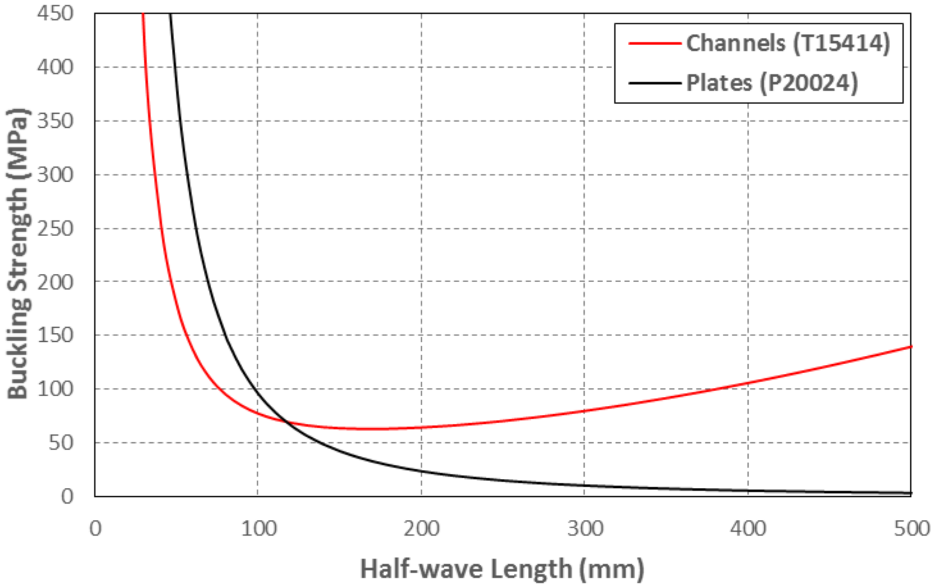

Figure 15: Signature curve of the components of columns SC1

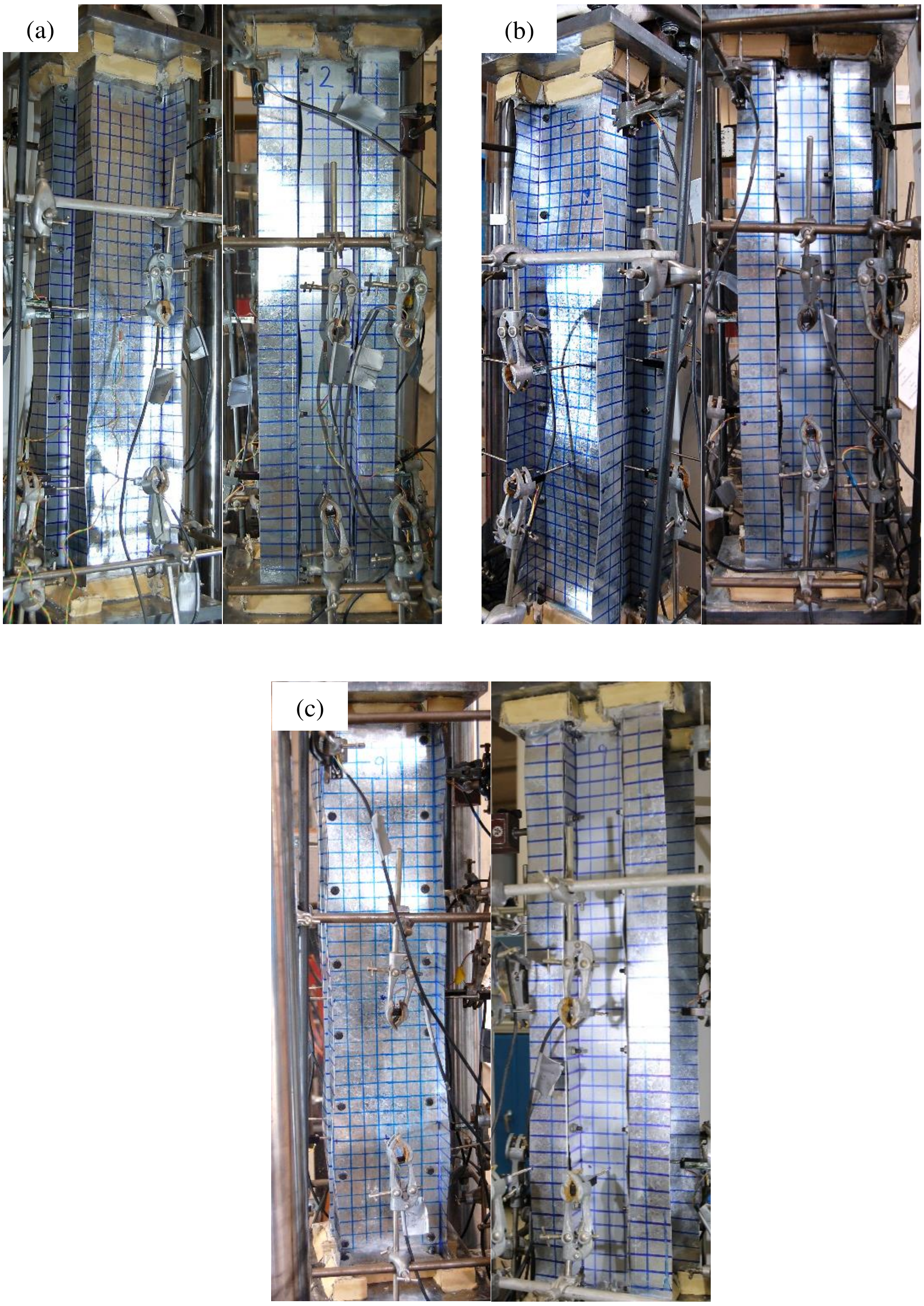

Figure 16: Deformed shape approaching ultimate load in a) SC2-2a, b) SC2-4a, c) SC2-6a

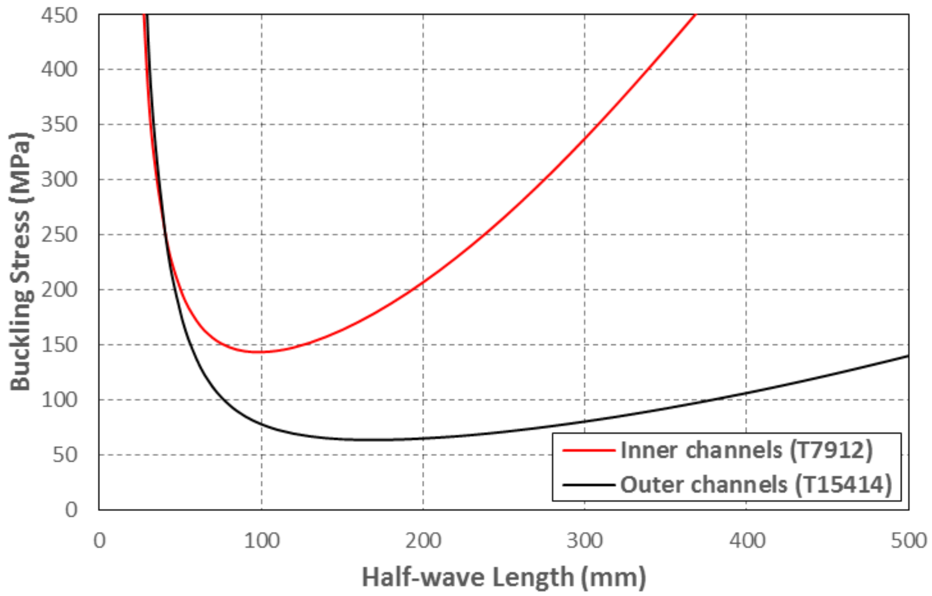

Figure 17: Signature curve of columns SC2

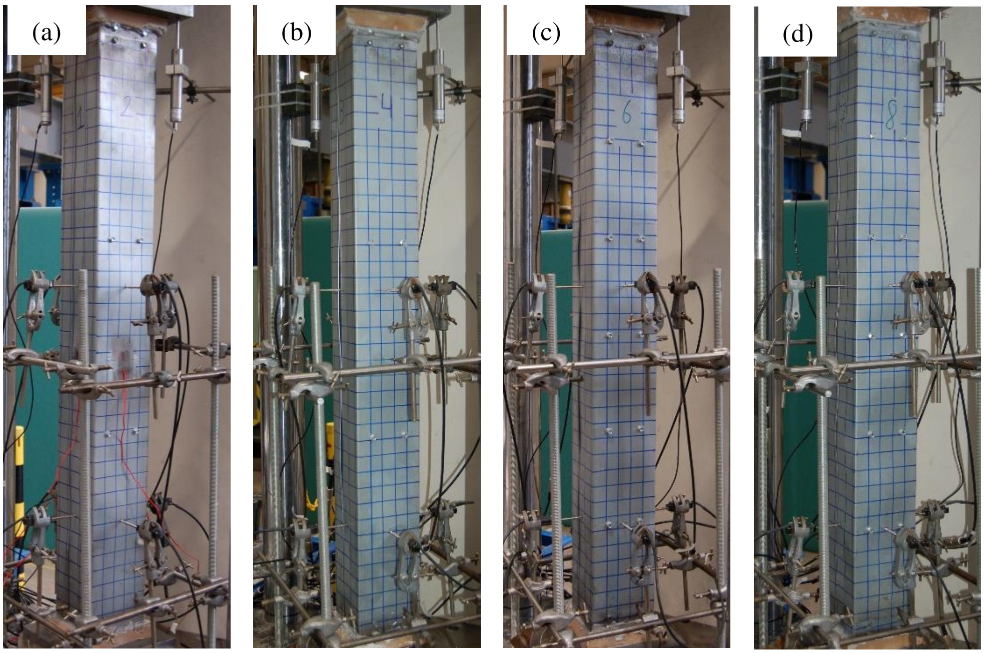

Figure 18: Deformed shape approaching ultimate load in a) SC3-2a, b) SC3-2b, c) SC3-5a, d) SC3-5b

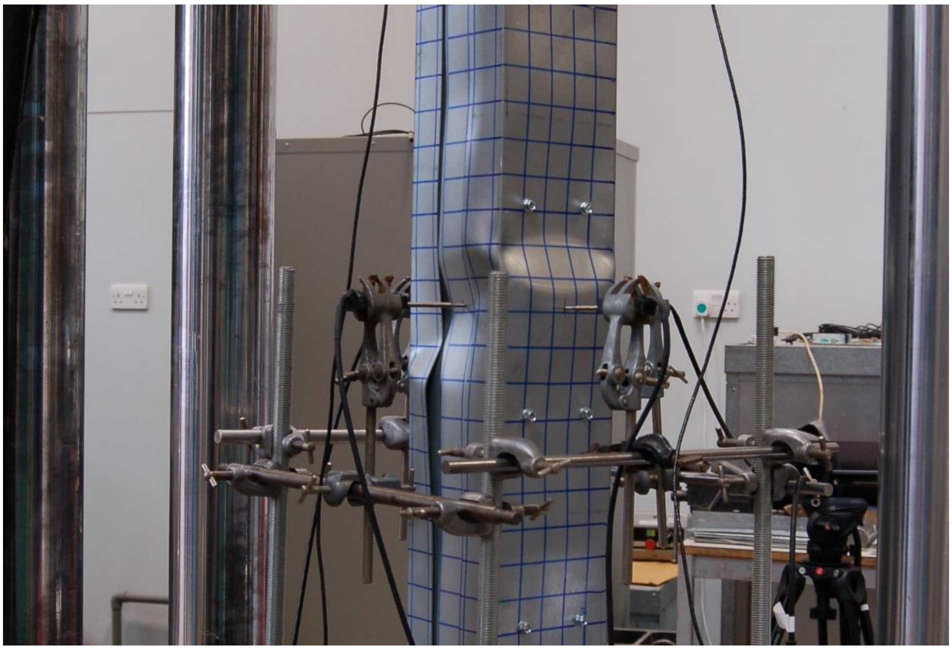

Figure 19: Localised failure mechanism in column SC3-5b

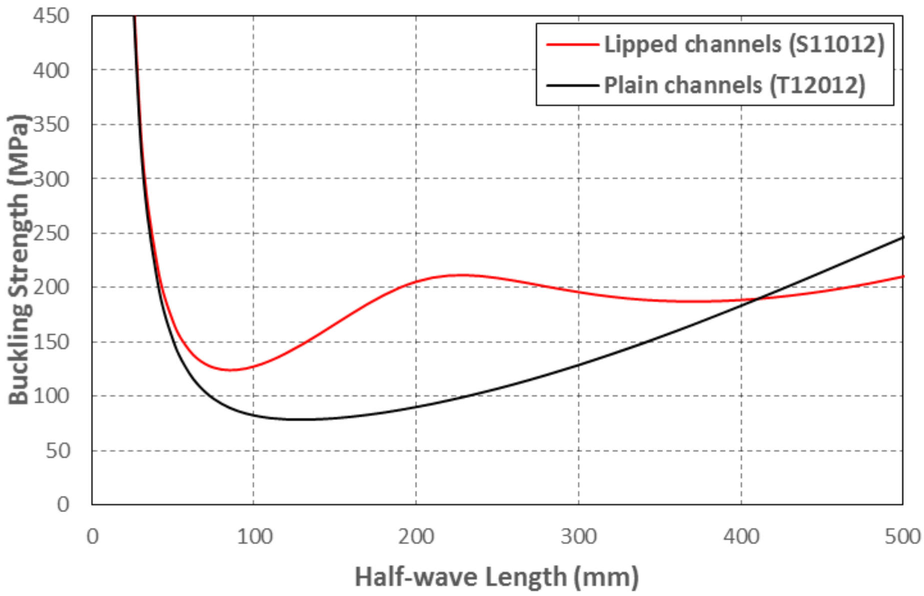

Figure 20: Signature curve of the components of built-up columns 3 and 4

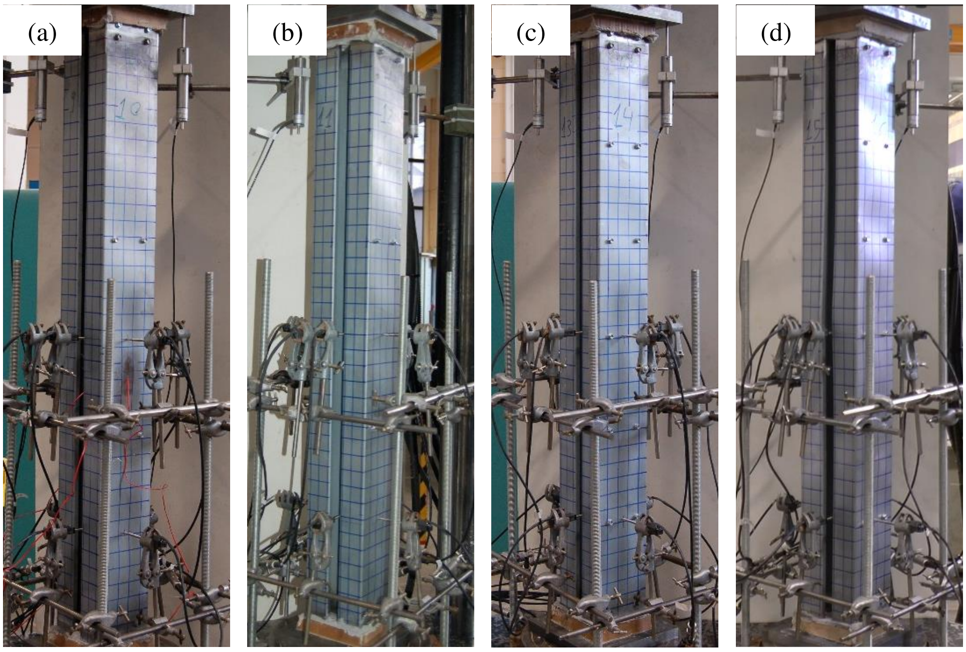

Figure 21: Deformed shape approaching ultimate load in a) SC4-2a, b) SC4-2b, c) SC4-5a, d) SC4-5b

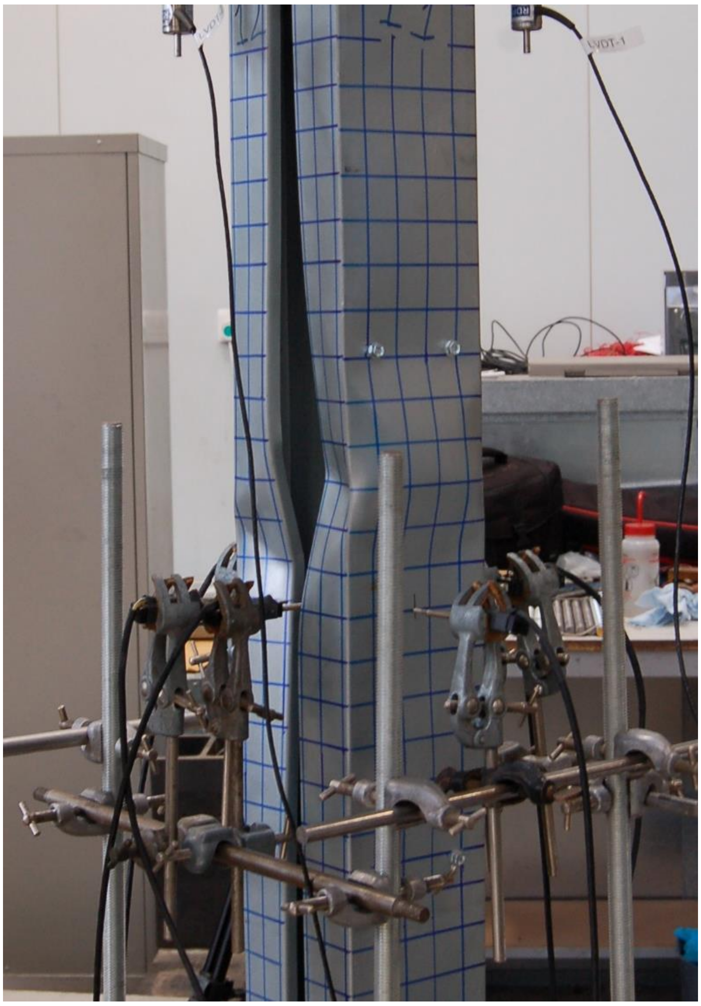

Figure 22: Localised failure mechanism in column SC4-2b

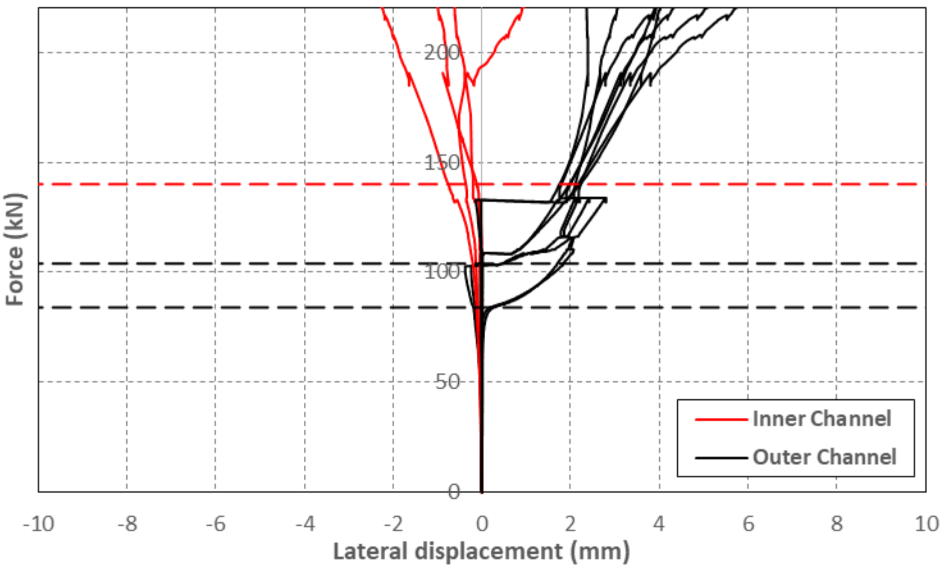

Figure 23: Axial load vs lateral displacements in SC2-2a

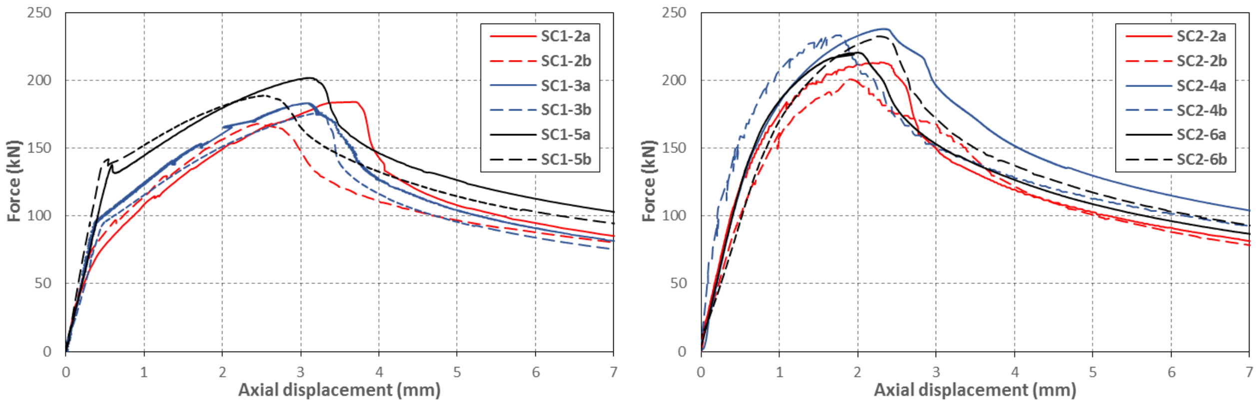

(a) (b)

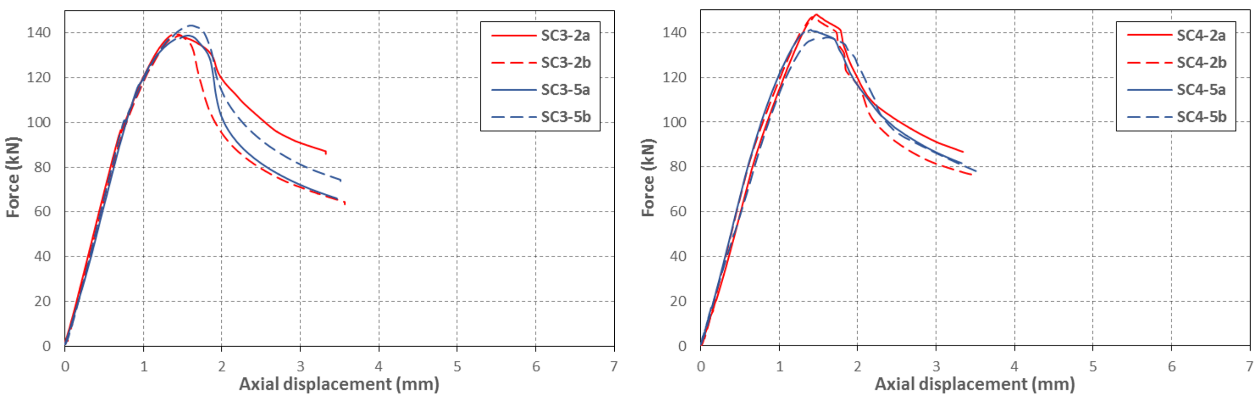

(c) (d)

Figure 24: Axial load vs. deformation curves for: a) columns SC1, b) columns SC2, c) columns SC3, and d) columns SC4